The Design and Fabrication of a Two-Layer Microfluidic Device for Studying Microtubules *In Vitro*

By

Matthew Rogers

Thesis

Submitted to the Faculty of the

Graduate School of Vanderbilt University

in partial fulfillment of the requirements

for the degree of

MASTER OF SCIENCE

in

Chemical and Biomolecular Engineering

May 13, 2022

Nashville, Tennessee

Approved:

Matt Lang, Ph.D.

Marija Zanic, Ph.D.

Acknowledgements

This work was partially funded through an NIH grant to M. Zanic (R35 GM1192552) and NSF ID 2018661 to M. Zanic. MRR was also supported by NIH T32 GM08320 and a VINSE pilot funding award. A portion of this research was conducted at the Vanderbilt Institute of Nanoscale Science and Engineering. The author would also like to acknowledge Alice Leach, David Schaffer, and the entire Zanic lab for their assistance and support.

TABLE OF CONTENTS

Page

LIST OF FIGURES

Figure **Page**

Chapter 1

Introduction and Background

1.1. Introduction to microfluidics

Since its inception in the late 20th century, the field of microfluidics has rapidly evolved into a pivotal tool for transforming the world. Predominately triggered by the revolutionary inventions of the transistor and integrated circuit, motivated by the requirements of molecular biology and molecular analysis, and further catalyzed by national security concerns of the United States' Defense Advanced Research Projects Agency (DARPA), microfluidics became the preeminent technology flexible enough to meet the demands of multiple interested parties in a wide array of fields [1–3].

The common factor in these applications was scale: small pieces of equipment that offered high efficiency testing without increased time or the added expense of precious reagents. Microelectronics were able to exponentially increase computational power and speed by the integration of multiple components on a single chip; molecular biology and analysis required precise control of inherently minute volumes of samples, such as DNA for amplification; and the preservation of national security was directed toward the ability to identify a biological or chemical attack using portable and relatively inexpensive detection devices [1,2,4–6].

Microfluidic technology focuses on the manipulation of small volumes of fluids, typically on the order of less than 10^{-6} liters, within fabricated channels with feature sizes on the order of micrometers [1,7]. However, while the primary desirable characteristic of microfluidic systems was the ability to efficiently control small amounts of precious reagents, it was not their only appealing

quality. The inherent nature of microfluidics also allowed for: high-resolution experimentation; precise manipulation of multiple reagents in parallel; a reduction in time and cost compared with assays that were not as sensitive or required more reagents; and rapid generation and iterative design improvement of the microfluidic systems themselves. Soon, microfluidics were being readily applied in biology and chemistry as a way to scale-down an entire laboratory process onto a single microfluidic device – the colloquial "lab-on-a-chip" [1,2,8–13].

Due to their intrinsically small size, microfluidic devices incur several interesting engineering phenomena. The Reynolds number, a dimensionless ratio between the inertial and viscous forces in a flowing fluid, is typically on the order of $O(10)$ or below in microfluidics, which results in linear, Stokes' flow where viscous forces dominate. Furthermore, the Peclet number, a ratio of convective to diffusive transport in mixing media, demonstrates that convective transport is typically negligible in microfluidics [14–16]. This Stokes'-driven, diffusion-mediated regime is advantageous, as it allows for multiple experiments to be run in parallel on the same device, precise gradients of solutions to be maintained, and the flexibility to design and robustly test several hypotheses in a well-controlled, highly efficient system.

This novel flexibility is due in large part to the fabrication of microfluidic devices themselves. Since the advent of modern photolithography in the 1950's for use in semiconductors, the technique has become the primary fabrication method for microfluidic devices (Figure 1) [2,17,18]. Traditionally, the photolithography process creates a 'master' of a microfluidic design, akin to how photographic film is used to create prints. In microfluidics, a photosensitive substrate is prepared on a silicon wafer, and a photomask of the microfluidic design is used to expose only the desired areas of photoresist to a radiation source, typically within the ultraviolet spectrum. Wet etching methods then develop the substrate to yield a relief of the microfluidic design. In this way, many

designs can be fabricated on the same silicon wafer, and features within the design can reliably be produced at resolutions nearing the wavelength of the exposure light, as low as 100 nanometer feature sizes [7,19]. After the creation of the relief master, (poly)dimethylsiloxane (PDMS) is often cast as a liquid elastomer and cured onto the master. The cured PDMS, which has adopted the negative features of the master's design, can then be removed. The PDMS is then bonded to a surface such as glass by using a variety of techniques, most common of which is surface bonding after activation by gas plasma. The complete fabrication can typically be performed in 1-2 days, allowing for high-throughput design iterations while also rapidly yielding multiple devices. Furthermore, highly complex systems can be included in the device design, including mixers, valves, integration with microelectronics, and more [16,20,29,30,21–28]. For more detailed reviews of the soft lithography and microfabrication processes, see the associated references [1,7,8,31–35].

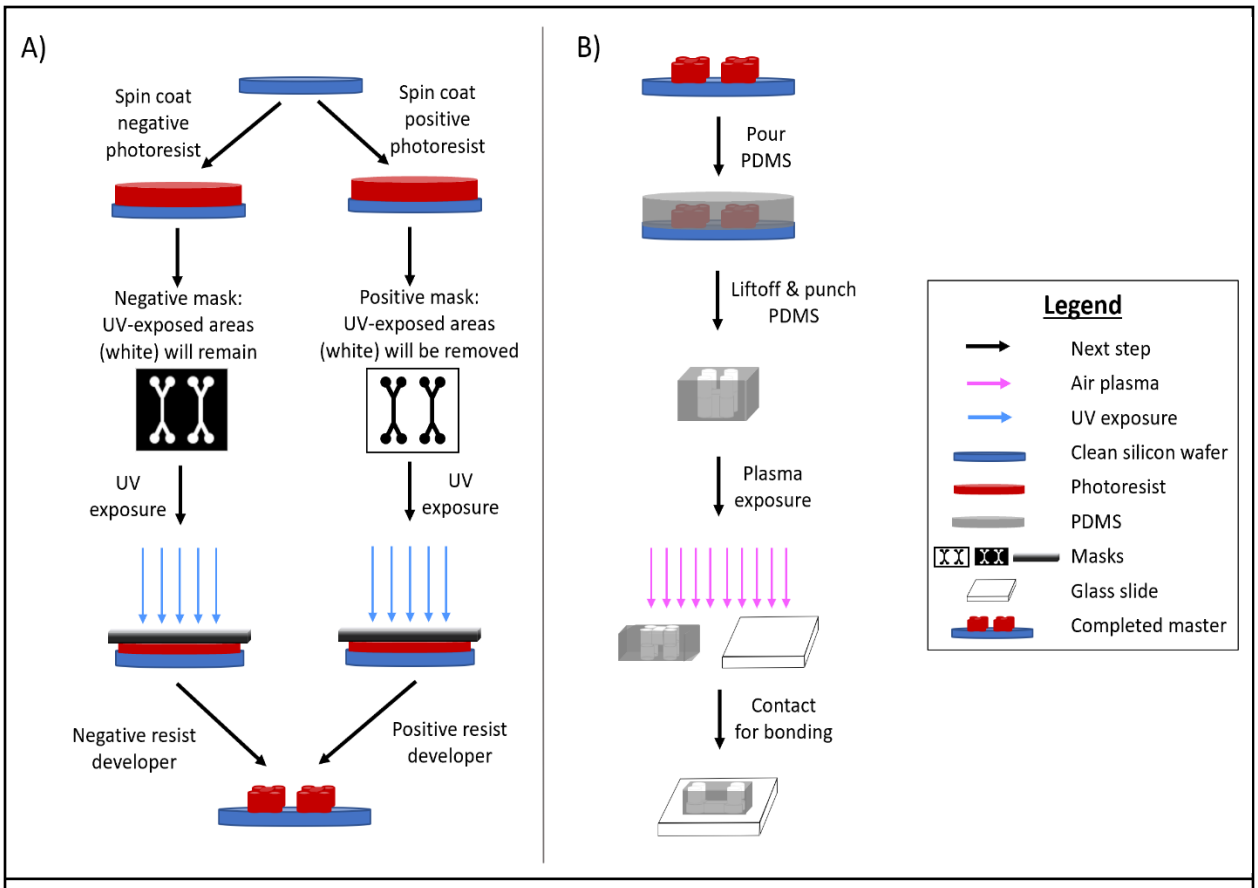

Figure 1. Overviews of the traditional photolithography process (A) and microfabrication process (B). Depending on the application and desired photoresist characteristics, a negative or a positive photoresist can be used, even though they will yield the same design master. Characteristics such as feature height desired or photoresist melting temperature help determine the appropriate photoresist type.

It is worth noting that the choice of PDMS as the traditional microfluidic device medium is not accidental. Its optical transparency, relatively low cost, high biocompatibility, relative chemical inertness, durability, and mechanical flexibility all lend desirable characteristics that allow PDMS-based microfluidic devices to be used in a myriad of scientific investigations [1,7,35–39,8–10,16,22,23,29,33].

However, it would be remiss to exclude the recent advances of other microfluidic applications, such as glass-based devices, paper-based devices for low-income and point-of-care diagnostic testing, and even autonomous, highly flexible soft robotics devices [38,40,49–51,41–48].

Moreover, microfluidic devices are increasingly applicable in various areas of the consumer marketplace, including pregnancy tests, diabetic monitoring supplies, and even the recent COVID-19 pandemic. Currently, the microfluidics market value is estimated at nearly $20 billion USD annually, with predictions of an annual market value of $60 billion USD by 2028 [50,52–54]. It is apparent, then, that microfluidic devices and their applications are incredibly impactful in multiple spheres. One of these spheres is cell biology, where the array of microfluidics-assisted investigations includes cancer, organ function (Organ-on-a-Chip), antibiotic-resistant bacteria, and even sperm motility [15,24,29,37,55–59]. More specifically, the lens of this thesis is focused on microfluidic applications to the field of microtubule biology.

1.2. Introduction to microtubules

As a major component of the cytoskeleton, microtubules are crucial to many cellular processes, including cell division and motor protein-mediated transport of intracellular cargo [60,61]. For example, during mitosis, microtubules arrange into a mitotic spindle to pull apart chromosomes into two daughter cells. Without this mechanical contribution from the microtubules, mitosis could not take place successfully [62]. In fact, this step in cell division has been successfully targeted by anti-cancer therapeutics to compromise microtubule function in cancerous cells and prevent their proliferation [63–66]. Furthermore, several other disease states, such as Alzheimer's and Parkinson's diseases, are also correlated with erroneous microtubule dynamics

and/or mechanics [67–70]. A better understanding of microtubules, then, can further our comprehension of the cellular architecture and facilitate more effective therapies.

Microtubules are hollow cylinders comprised of protofilaments of tubulin heterodimers, which have an α-tubulin and β-tubulin subunit bound together in a head-to-tail fashion. Polymerization of heterodimers into protofilaments occurs spontaneously when a guanosine triphosphate (GTP)-bound tubulin dimer bonds to a pre-existing microtubule polymer, or to a microtubule template such as a microtubule organizing center *in vivo*. The GTP is hydrolyzed to guanosine diphosphate (GDP) shortly thereafter, resulting in GDP-bound tubulin subunits comprising the majority of the polymer lattice [71,72]. In humans, the microtubule lattice is canonically comprised of thirteen protofilaments, but the number of protofilaments can vary wildly among different species – and can even vary within a single species [73]. Moreover, microtubules can polymerize from both ends of the polymer, albeit at different kinetic rates. The faster growing end is designated as the 'plus' end, while the slower growing end is the 'minus' end [74]. This polarity is important for several processes, namely intracellular transport, where certain families of motor proteins are directed exclusively to one end of the microtubule [75]. Furthermore, either microtubule end can spontaneously switch to a phase of depolymerization, known as a 'catastrophe'. If the microtubule recovers and resumes growing, it has achieved a 'rescue'. Microtubules often switch between these states sporadically, resulting in a stochastic process known as 'dynamic instability' (Figure 2) [74,76].

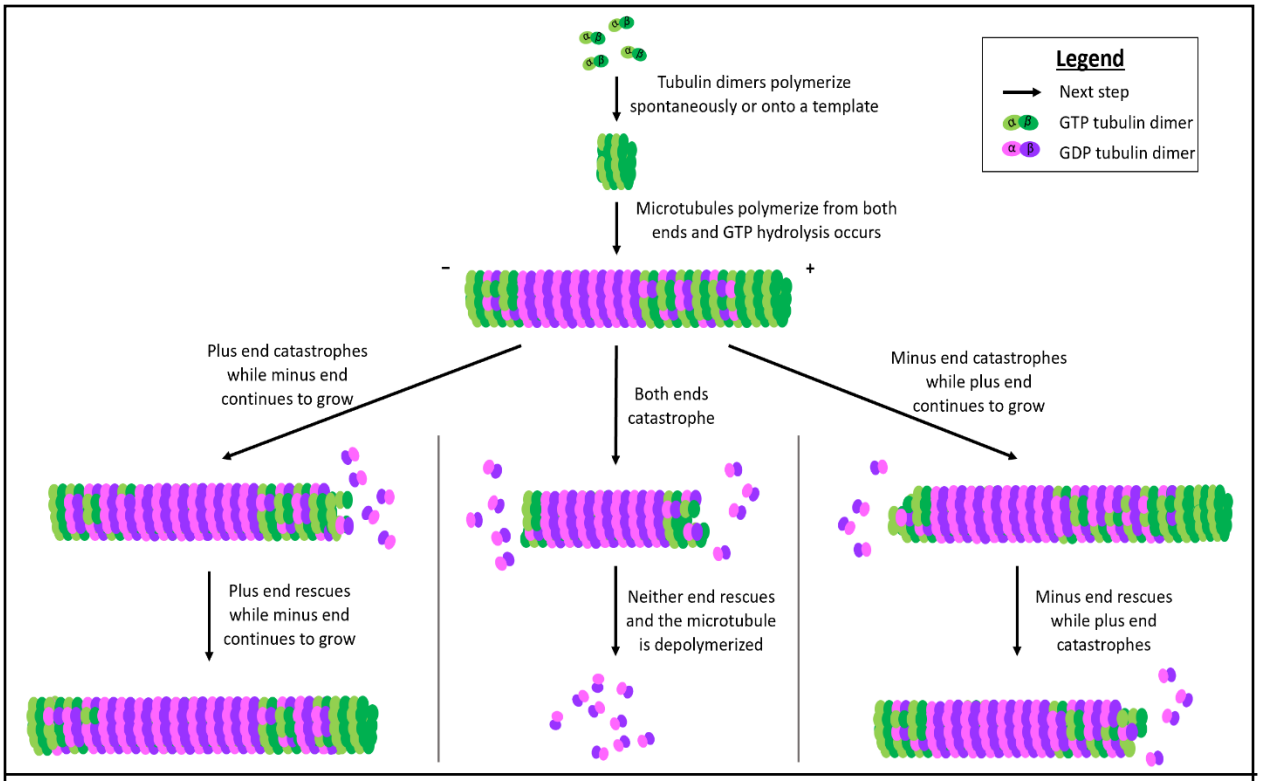

Figure 2. Overview of stochastic dynamic instability. Note that the three pathways depicted here are not the only outcomes that microtubules may have during their lifetimes; these are merely examples to demonstrate the interplay between concurrent kinetic rates of GTP hydrolysis and tubulin dimer attachment/detachment at the microtubule ends.

Microfluidic devices have been adopted to further investigate the dynamic and mechanical properties of microtubules and their higher-order structures *in vitro*. A range of microfluidic devices has been created to: probe the dynamic instability and kinetics of microtubule polymerization; examine microtubule-microtubule interactions; re-create the mitotic spindle in cell-like spherical suspension droplets; investigate the role of microtubule associated proteins (MAPs), such as kinesins, in microtubule stability and transport; and explore the biomechanical properties of microtubules, such as flexural rigidity and bending stiffness [77,78,87–93,79–86].

However, while there have been significant contributions to the field due to the advancements made by microfluidics, there are still areas for improvement. Three specific issues are: the potential for air bubbles in the microfluidic channels, lack of robustness due to manual manipulations of the microfluidic devices, and the underutilization of higher-throughput assays using microfluidics.

In many biological applications, air bubble formation within a flow cell is catastrophic, as air bubbles can denature proteins, shear microtubule polymers, and adversely affect cell cultures [94,95]. While microfluidic devices are an improvement over more traditional flow cell designs, microfluidics still have limitations with air bubbles that form for a variety of reasons. Air bubbles can form in microfluidic channels due to repeated plugging in and unplugging of tubing attached to the device, or due to the presence of surfactant solutions in the device. Furthermore, sharp corners or oblique angles in the device design can result in fluids non-uniformly traversing the channels, which increases the possibility of air entrainment in a device. Many techniques have been created to minimize the formation, persistence, and impact of bubbles, but the overall inclusion of bubble mitigation techniques is by no means universal [94–98].

Furthermore, manual interventions such as tubing manipulation introduce not only the potential for bubble formation, but also the possibility of other undesirable consequences. These consequences can include cross-contamination of reagents in the device, physical damage to the device itself, and unintended pressure-driven flow within the device. This last point identifies a more specific area of improvement for microfluidic systems that utilize fluid flow profiles for applications: it is challenging to consistently reproduce a fluid velocity profile when introducing a solution by hand using a pipet or a manually adjusted flow valve. For example, a consistent flow profile is crucial when investigating the gradual change in flexural rigidity of microtubules

subjected to repeated oscillatory flow. While some applications have included fluorescent beads in solution to calculate the local flow velocity experienced by a bending microtubule, the local drag forces on the beads, the potential for the beads to stick to the surface of the microfluidic channel, and the potential for beads to impact the microtubules themselves can result in threats to the internal validity of the measurements [77,80,81,88,91].

Finally, as previously mentioned, the intrinsic advantages offered by microfluidic devices can allow for higher-throughput, more efficient testing than traditional flow cell assays. To reduce waste, save time, and more efficiently use reagents that are expensive and difficult to prepare, microfluidic devices can be designed to test multiple experimental conditions in parallel on the same device. An example of this would be creating a device that partitions different areas of the same channel for testing the effect of differing concentrations of tubulin on dynamic instability of the microtubules located in each area.

This thesis focuses on these three major areas of improvement by creating a two-layered microfluidic device to be used for several microtubule-based applications. The proposed device incorporates redundant bubble trapping capabilities, includes a diaphragm valve system to prevent unintentional fluid flow or contamination of reagents, and interfaces with an automated flow control system with an in-line rotary valve to reduce manual intervention, while also enabling different gradients of solutions in different areas of the device for high-throughput analyses. Moreover, both COMSOL Multiphysics (COMSOL, Inc.) and MATLAB (MathWorks) software are utilized to better develop and understand the fluid transport and microtubule mechanics investigated using this system. Overall, the engineering of this microfluidic flow system can help researchers further understand microtubule mechanics and can provide improvements to experimental design in the broader microtubule field.

Chapter 2

Materials and Methods

Note: Since the design and fabrication processes were a primary objective of this thesis, much of the process development and associated data are detailed in the Results and Discussion chapters of this thesis, but the equipment used is described here.

2.1. Photolithography and microfabrication

All photolithography and microfabrication were performed in the Vanderbilt Institute of Nanoscale Science and Engineering (VINSE).

Prior to use, 3" single side polished silicon wafers (UniversityWafer, Inc.) were cleaned using a Trion Phantom II cleaner with oxygen plasma (Trion Technology, Inc.) and then were silanized with hexamethyldisilazane (HMDS) using a 310TA HMDS Vapor-Prime/Image-Reversal Vacuum Oven (Yield Engineering Systems). MEGAPOSIT™ SPR™ 220 7.0 photoresist (Dow, Inc.) was spin-coated at varying thicknesses (5-20 μm) onto the silicon wafers. The microfluidic masks were designed using AutoCAD (Autodesk) and fabricated in etched glass by VINSE personnel. The device masks were aligned and exposed onto the SPR 220-coated silicon wafers by using a Karl Suss MA-6 platform (SUSS MicroTec). MICROPOSIT™ MF™-319 developer (Dow, Inc.) was used to remove residual photoresist. To facilitate future elastomer liftoff, developed device masters were then silanized for 2 hours under vacuum using trichloro(1H, 1H, 2H, 2H-perfluorooctyl) silane (MilliporeSigma).

Liquid (poly)dimethylsiloxane (PDMS) elastomer and associated curing agent (Dow, Inc.) were hand mixed in a 10:1 weight ratio for 5 minutes, desiccated for 30 minutes, and then were cast on device masters. The cast PDMS was allowed to cure on the device masters at 65 ˚C overnight. The cured PDMS was removed from the device masters using a standard scalpel and tweezers, and inlet and outlet holes were punched in the PDMS using a standard 1.5 mm biopsy punch (Integra LifeSciences). Profilometry of the device masters and PDMS was performed using a KLA Tencor P-7 stylus profilometer (KLA Corporation) using a maximum scan height of 327 μm and a needle force of 0.5 mg. Two-layer PDMS-PDMS alignment was assisted by a custom PDMS alignment tool, which utilized ThorLabs motion control (ThorLabs, Inc.) and Dino-Lite optics and software (Dino-Lite). Once aligned, two-layer PDMS-PDMS plasma bonding was achieved using a PDC-32G Plasma Cleaner (Harrick Plasma) with attached vacuum line and clean, dry air (CDA) plasma. For PDMS-glass plasma bonding, 18x18 mm coverslips were wiped with isopropyl alcohol (IPA) and plasma cleaned for 5 minutes using the same CDA plasma system. Finally, each aligned and bonded two-layer PDMS device was bonded to one of the 18x18 mm coverslips using the same CDA plasma system.

Quake valve performance was demonstrated with a custom microfluidic flow control system which utilized Fluigent LineUp™ series flow controllers and associated equipment (Fluigent), as well as a SMZ-168 Stereomicroscope with Moticam 5+ for digital image capture (Motic).

2.2. Tubulin preparation

Bovine brain tubulin was purified using the high-molarity buffer method using cycles of polymerization and depolymerization of tubulin from bovine brains [99]. Tubulin was labeled with

Alexa Fluor 488 or Alexa Fluor 647 (Invitrogen) according to the standard protocols, as previously described [100]. Fluorescently labeled tubulin was used at a ratio of between 5% and 10% of the total tubulin when growing dynamic microtubule extensions.

2.3. Introduction, growth, and stabilization of microtubules in microfluidic device

Once microfluidic devices were fabricated, the preparation of the microfluidic channels for microtubules consisted of a BRB80 wash (80 mM piperazine-*N*,*N*′-bis(2-ethanesulfonic acid), 1mM $MgCl_2$, and 1mM EGTA at 6.8 pH), a 5-minute incubation with anti-tetramethylrhodamine antibody (Thermo Fisher Scientific), another BRB80 wash, a 15-minute incubation with Pluronic® F127 poloxamer (MilliporeSigma), and a final BRB80 wash, as previously described [100].

For growing microtubules, tetramethylrhodamine-labeled guanosine-5'-[(α,β)-methyleno]triphosphate (GMPCPP)-stabilized microtubules ('seeds') were first prepared according to standard protocols (rhodamine labeling ratio was ~25%) [100,101]. GMPCPP is a slowly hydrolyzable analog to GTP, allowing for stabilized microtubule seeds; while these microtubules will depolymerize over an extended period of time (i.e. several hours), they are not subject to dynamic instability. Microtubule seeds were then introduced to the microfluidic device and allowed to bind to the glass coverslip via the anti-rhodamine antibody. Unbound microtubule seeds were washed away with BRB80 and an imaging buffer. This imaging buffer (anti-fade solution) was used to prolong photostability of the system and consisted of BRB80 supplemented with 40 mM glucose, 40 μg/mL glucose oxidase, 16 μg/mL catalase, 0.5 mg/mL casein, 50 mM KCl, and 10 mM DTT. Using a final concentration of 14-18 μM 488-nm labeled tubulin, dynamic microtubule extensions were then polymerized from surface-immobilized GMPCPP-stabilized templates as previously described, supplementing the tubulin solution with 1 mM GTP in imaging

buffer [100,101]. Finally, stabilization of microtubule extensions was achieved by flowing in 10 μM paclitaxel (Taxol®, Tocris Bioscience) in imaging buffer.

2.4. Fluorescent microscopy

All flourescent microscopy was performed using Total Internal Reflection Fluorescence (TIRF). Imaging of microtubules *in vitro* was performed using a custom brass stage adapter to fit the microfluidic device onto a Nikon ECLIPSE Ti microscope equipped with a 100×/1.49 numerical aperture TIRF objective (Nikon); Andor iXon Ultra EM-CCD (Electron-Multiplying Charge-Coupled Device) and Andor NEO sCMOS (scientific Complementary Metal-Oxide Semiconductor) camera (Oxford Instruments); 488-, 561-, and 640-nm solid-state lasers (Nikon); HS-625 high-speed emission filter wheel (Finger Lakes Instrumentation); and standard filter sets. An objective heater (Tokai Hit) was used to maintain the sample at 35 °C. Images were acquired using NIS-Elements (Nikon). Microtubule growth was imaged for 15 minutes, imaging the 488-nm channel every 5 seconds and the 561-nm channel every 1 minute. Microtubule stabilization by Taxol® was verified by imaging for 10-15 minutes after Taxol® washout. When bending microtubules, the 488-nm channel was imaged every 0.1 seconds and the 561-nm channel every 10 seconds. Images were analyzed using open access ImageJ software [102,103].

2.5. Automated flow control

Automated flow control was achieved using an OB1 MK3+ microfluidic flow controller in combination with 0-80 μL microfluidic flow sensors, a MUX Distribution rotary bidirectional microfluidic valve, and Elveflow Smart Interface (ESI) software (Elveflow). Flow controller inlets used 1/16” outer diameter, 0.007” inner diameter PEEK resistance tubing (Thermo Fisher

Scientific), but all downstream connections into the microfluidic devices used 1.5 mm Tygon® tubing (Saint-Gobain), to match the 1.5 mm biopsy punch hole size from microfabrication. Interconnections between PEEK resistance tubing, flow controllers, and Tygon® tubing were made using flangeless PFA fittings with ETFE ¼"-28 to 1/16" outer diameter ferrules (IDEX Health & Science, LLC). Custom recipes for flow control were also created using the ESI software.

2.6. Computational modeling and analysis

Fluid flows and concentration gradients within the microfluidic design were modeled in COMSOL Multiphysics (COMSOL, Inc). Lastly, a MATLAB (MathWorks) custom script was used with experimental data to characterize microtubule bending profiles and flexural rigidity. The main text and Appendix C detail the analysis method and associated MATLAB script.

Chapter 3

Results and Discussion, Fabrication of Microfluidic Device

3.1. Microfluidic device design rationale

As mentioned in the Introduction chapter, our microfluidic device was designed considering several key factors. An AutoCAD schematic of the final, two-layer device can be seen in Figure 3, while our design rationale is detailed below. It should also be noted that our OB1 microfluidic flow controller was equipped with two regulating channels. More channels can be purchased and implemented, but for our proof-of-concept design, we operated under the assumption that only two inlet/outlet ports would be under pressure control at any one time.

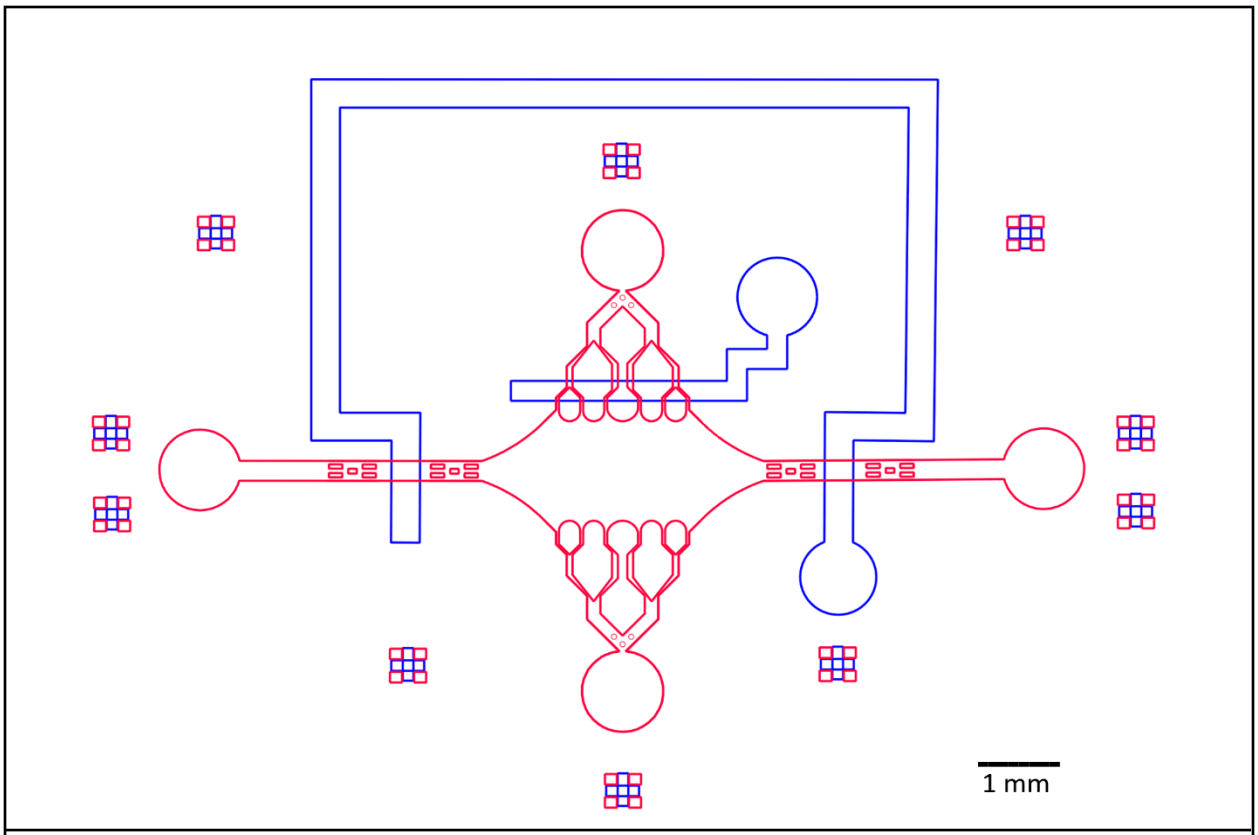

Figure 3. AutoCAD schematic of our microfluidic device design. Two separate devices are fabricated and then overlayed. The bottom layer (red) contains microtubules (not shown) and all solutions. The top layer (blue) functions as a diaphragm valve when pressurized with air. Rectangular markings on the periphery are for alignment of the two layers.

First, we wanted a large, rectangular chamber which would house the microtubule seeds and their extensions and would serve as the main area for imaging. This chamber would be intersected on each side by a flow channel. Along the abscissa of the central chamber, straight channels would serve as an inlet and outlet to facilitate rapid solution exchange. Microtubule seeds would be introduced to the chamber and laminar flow would ideally result in the seeds binding to the glass surface in the x-plane, along the direction of flow. Along the ordinate of the central chamber, the flow channels sequentially branched into smaller channels until reaching the

chamber, similar to other designs [77,80,88,91]. The feature of branching channels was proposed for studying the biomechanical properties of microtubules; by branching the channels and flowing solution perpendicular to the microtubule seeding orientation, a near-normal bending force could be imparted on the microtubule extensions through a wide area of the central chamber. This contrasts with a design that has only a single channel flowing solution into the central chamber, where the local velocity field would not be as homogenous, resulting in more varied forces applied to the microtubules. In our device, since the flow profiles exiting each branching segment would be similar, comparable forces would be imparted onto a larger area of microtubules. Therefore, the branching motif, while seemingly more complicated, can reduce overall complexity in determining force imparted to microtubules without the added cost of requiring more reagents. Figure 4 shows this comparison in a COMSOL simulation. A design in this fashion also results in multiple lines of symmetry, allowing for ease of use and the opportunity to evaluate bending from multiple sides of the microtubule.

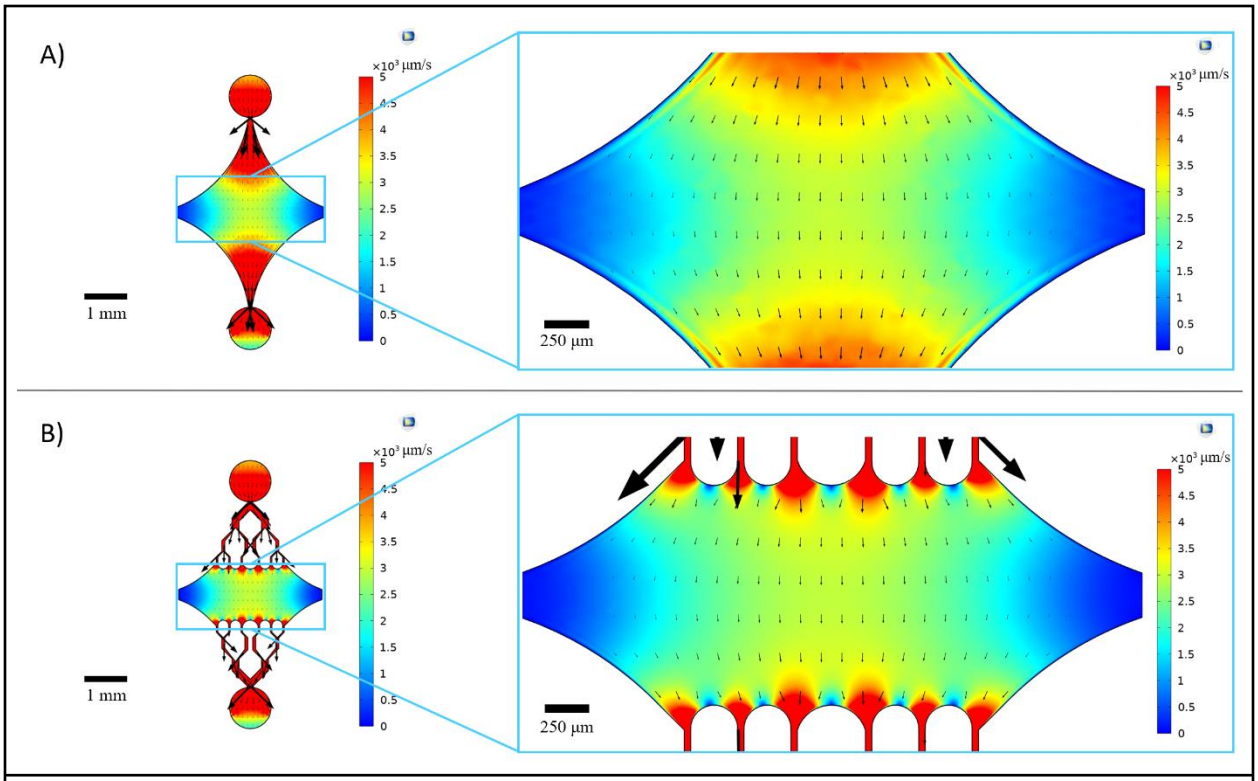

Figure 4. Inclusion of a branching motif results in a large area of similar flow. COMSOL simulations of two device designs under steady state flow: one without branching channels (A) and one with branching channels (B). Arrows denote local flow direction and are proportional to flow magnitude. Surface coloration denotes centerline velocity. Images on the right show zoomed in section of the device where microtubules (not shown) oriented along the x-axis would be subject to bending forces from a fluid flowing in the top port and out the bottom port. Left and right ports of the device would be blocked off via diaphragm valve. Incorporating branching channels increases the relative area subject to similar velocity fields while not increasing the volume of reagent required.

Platforming from the ability to assess bending from multiple sides of the microtubule, we wanted this device to be capable of simultaneously testing multiple experimental conditions. In some cases, this would require sequestering areas of the device to prevent non-uniform fluid flow

or to prevent solution cross-contamination. To address this, we incorporated a set of PDMS-based, diaphragm-like valves, colloquially known in microfluidic applications as 'Quake valves' [26]. Traditionally, diaphragm valves function in a process line by raising or lowering a flexible diaphragm membrane to block a flow path. This can be indirectly achieved in microfluidic devices by using a two-layered microfabrication approach. The 'valve' is created from its own microfluidic master using photolithography and cast in PDMS. However, in this case, the 'valve' is designed so that when it is aligned perpendicularly on top of another microfluidic device, the valve overlays a flow channel of the microfluidic device below. The valve can then be inflated, pushing down on the PDMS of the channel below and effectively sealing off the channel. Another benefit of this valve incorporation is the opportunity to save reagents by reducing the effective volume required within the device's area of interest.

Finally, we also wanted to include a series of bubble traps in our flow channels, in order to prevent air bubbles from reaching the central chamber. While numerous techniques have been shown to effectively prevent or mitigate the impact of bubbles, we opted to include arrays of micropillars within the flow path which would block air bubbles from traveling past due to surface tension [98]. Furthermore, to prevent air entrainment, all edges inside the device were designed as smooth curves rather than oblique angles. Combined, these precautions will reduce the possibility of air bubbles and increase the robustness of our design.

3.2. COMSOL gradient demonstration

We also performed COMSOL simulations on this design to demonstrate feasibility of using this device for high-throughput experiments. Along with the pre-mentioned capability of bending microtubules in multiple directions due to the device's symmetry, COMSOL simulations suggest

the potential to maintain precise gradients in the device, allowing for multiple experimental conditions to be run simultaneously (Figure 5). This efficiency can reduce time and waste while improving experimental robustness. For example, the effect of different proteins, or different concentrations of the same protein, on microtubule dynamics can be investigated simultaneously in the same device, and experiments could further include those proteins' effects on microtubule mechanics.

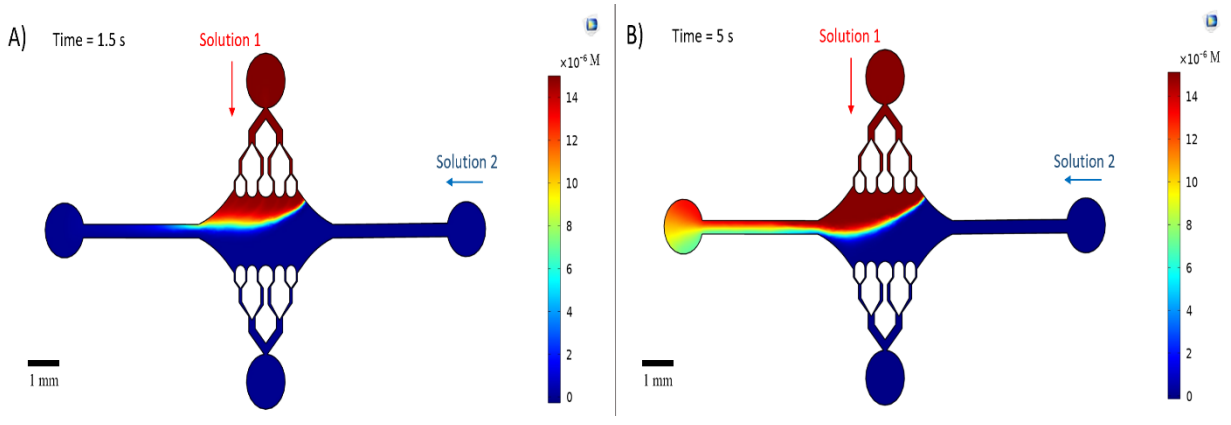

Figure 5. COMSOL simulation of the establishment (A) and maintenance (B) of a gradient of two solutions entering the device at the same inlet pressure (50 mbar) and initial concentration (15 μM). Inlet ports for each solution are denoted with colored arrows, and the two remaining ports serve as outlets. Heatmap shows the concentration profile of the top solution. Steady state was achieved at t = 5 seconds.

3.3. Microfluidic device fabrication

Once the device was designed, the development of a procedure to fabricate this microfluidic device system was a major milestone for this thesis. The finalized step-by-step

procedure for photolithography and microfabrication is included in Appendix A, while the primary outcomes are detailed below.

3.3.1. Diaphragm valve demonstration

First, we wanted to demonstrate proof-of-concept for a diaphragm valve system to block fluid flow. To do this, two straight microfluidic channels were overlayed perpendicularly. The bottom channel had both an inlet and an outlet punch hole for liquid flow, while the top channel had just one punch hole, effectively creating a dead-headed channel. A colored fluid was flown at constant upstream pressure through the bottom channel, and the top channel was pressurized at differing setpoints. Figure 6 shows a demonstration of this. As expected, inflating the PDMS between the two channel layers resulted in blockage of the flow path, with more pressure resulting in more efficient blockage.

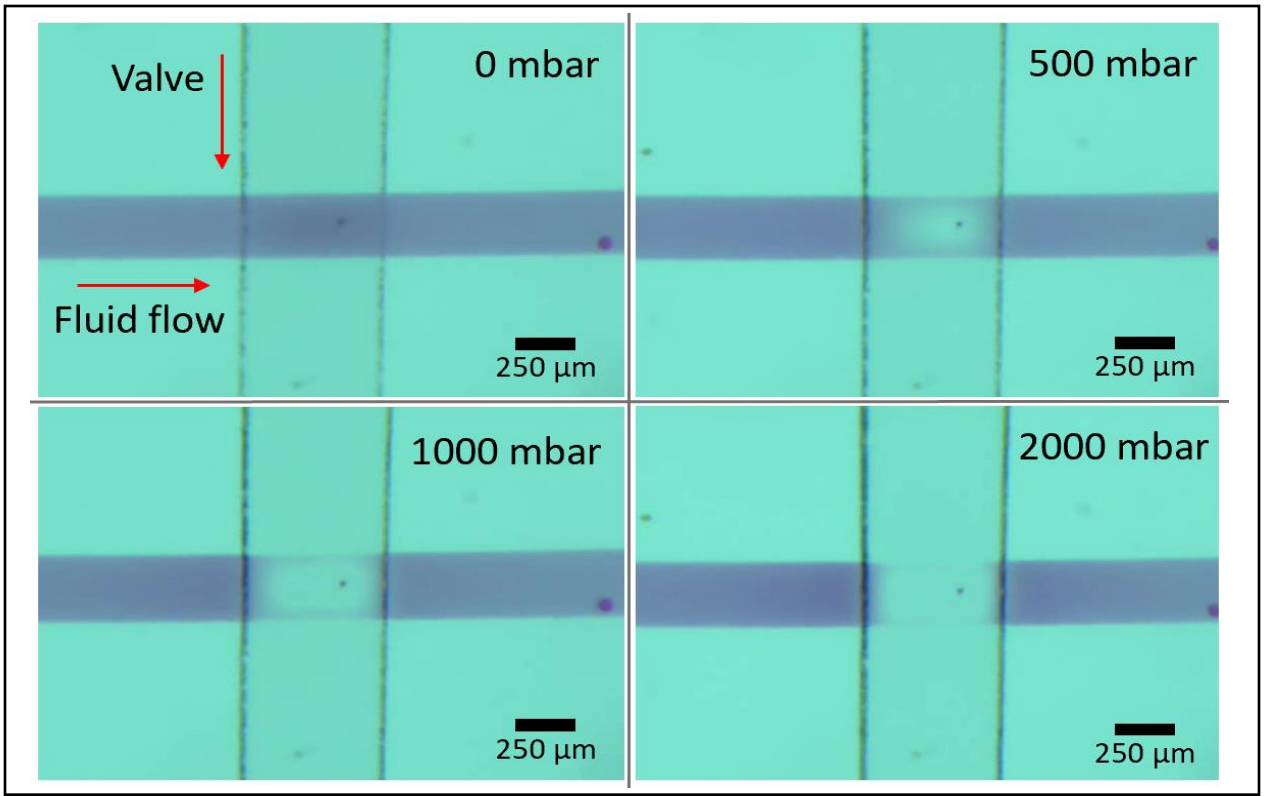

Figure 6. Increasing Quake valve pressure results in more efficient channel closure. Fluid at a constant upstream pressure (50 mbar) flowing through a channel can be blocked by pressurization of the overlaying Quake valve (top right of each image).

3.3.2. Creation of rounded channels

While our previous demonstrations showed our capability to create functional Quake valves, it has been shown that the rectangular profiles of features created in traditional photolithography are not ideal for complete closure of the flow channel, and that rounded flow channels achieve better sealing capabilities [104]. However, making the photoresist curved rather than rectangular is a non-trivial process, since the photoresist is traditionally exposed to light from above in a unidirectional manner.

As a result, we adopted a positive resist reflow technique using a relative low melting point photoresist, SPR 220. In a resist reflow, the device master is created using standard photolithography procedures, but then the developed photoresist is heated to its transition temperature. The surface tension of the photoresist results in the edges of the channels, which had previously been rectangular, to cohere and form a more rounded morphology. This method has been shown to create rounded channels in SPR-based designs with high success [104]. Our experiments were able to demonstrate this, as shown in Figure 7. While the smaller channels adopted very well-rounded profiles upon reflow, the wider channels were not as homogenous. Instead, the wider channels rounded near their edges as expected, but this rounding did not propagate to the entire channel, resulting in some of the channel remaining flat. This could be due to the cohesive properties of the photoresist or to the time allowed for reflow. These results suggest that a resist reflow technique can achieve well-rounded features in smaller channels, but wider channels may be less susceptible to this technique [104]. A potential improvement is to redesign the device master using thinner channels in some areas of the device, or empirically determine if resist reflow time or temperature parameters can be modified to yield rounded features in wider channels. More testing will also be needed to determine the effect of these reflow properties on valve efficacy.

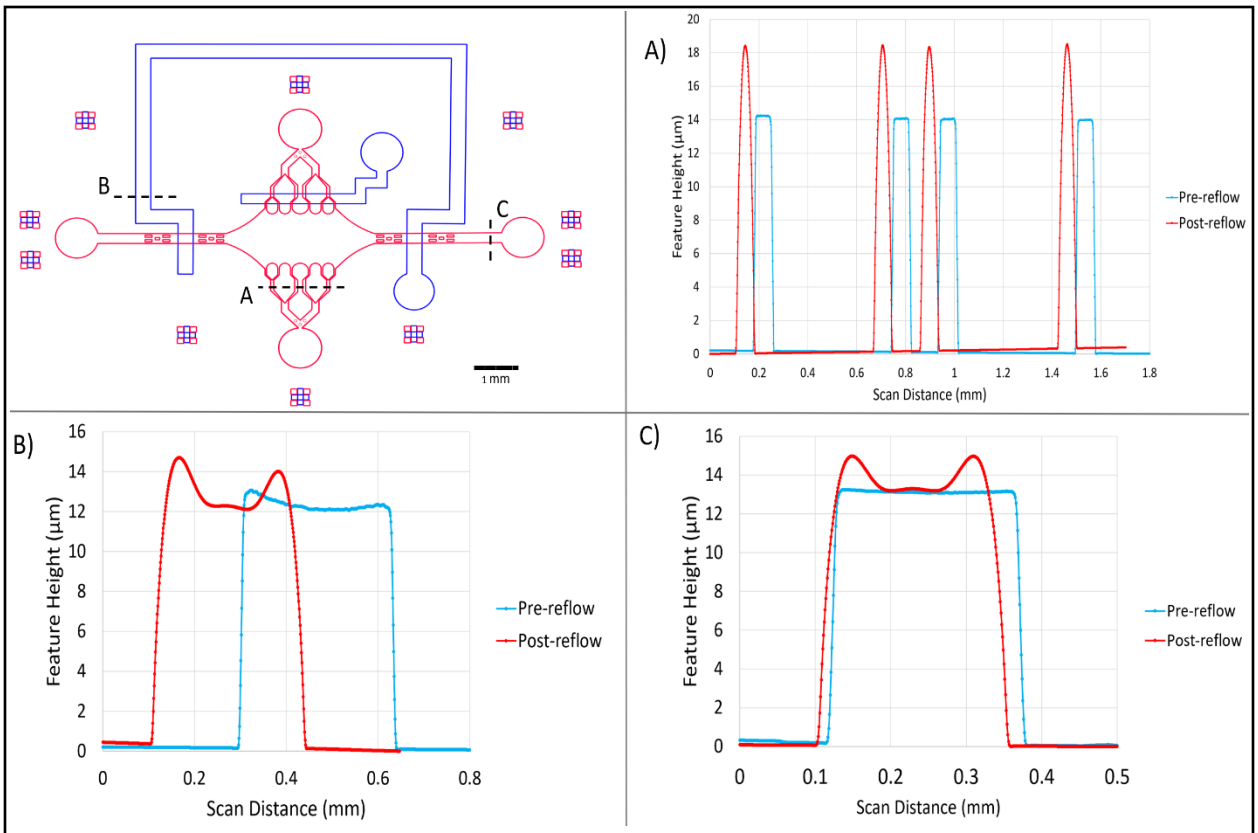

Figure 7. The resist reflow technique succeeded in rounding thinner channels. Top left: AutoCAD schematic annotated with three dashed lines (A, B, and C) indicating the profilometry scans (dashed lines not to scale). Top right: branching segments of device channel. These thinner channels resulted in more rounded, and taller but slightly thinner, motifs. Bottom left: wide section of valve. Bottom right: wide section of device channel.

3.3.3. Microfabrication and two-layer alignment

Once the device masters had been fabricated, two-layer PDMS alignment was the next stage gate. We developed a microfabrication procedure (Appendix A) that enabled us to attain a high success rate for appropriate alignment of the channel and valve PDMS layers. To contrast with the traditional processing steps described in Figure 1, an overview of our modified procedure is shown in Figure 8.

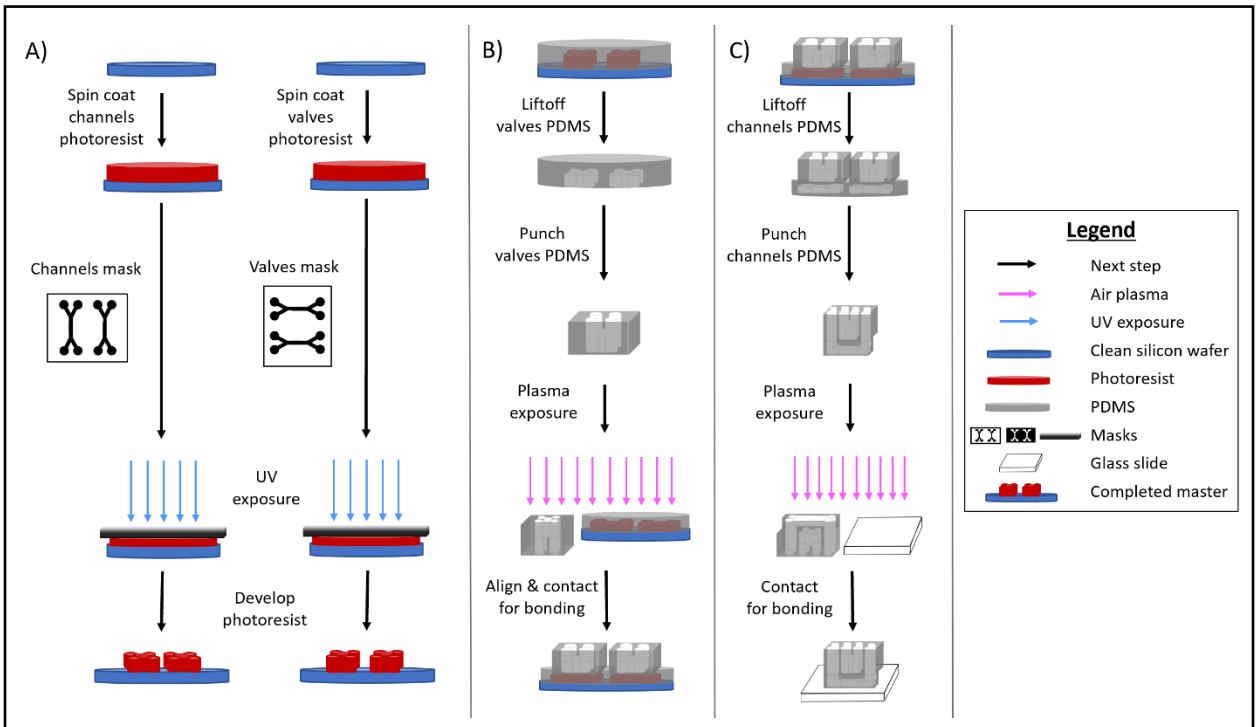

Figure 8. Overview of our modified photolithography and microfabrication protocols. A) Fabrication of the top, Quake valve master and the bottom, primary channel master. PDMS deposition and curing not shown. B) Valve PDMS removal, punch holes, and two-layer alignment and PDMS-PDMS plasma bonding. C) Primary channel PDMS removal, punch holes, and PDMS-glass coverslip bonding.

When developing this process, we found that the limiting step was the liftoff and manipulation of the bottom, primary channel PDMS. We determined that while a thicker layer of PDMS resulted in a more easily manipulatable device, a thinner layer of PDMS better facilitated sealing of the flow channel, as the force required to block the flow channel decreases with decreasing membrane thickness [26]. As a result, we aimed to spin-coat the primary channel master with a 40 μm layer of PDMS, based on previous findings [26]. We were able to achieve this thickness

by spin-coating PDMS at 2000 RPM for 30 seconds (Appendix A). Figure 9 shows an example profilometry scan. With this setup, our device's internal volume, as measured by COMSOL, was approximately 130 nanoliters.

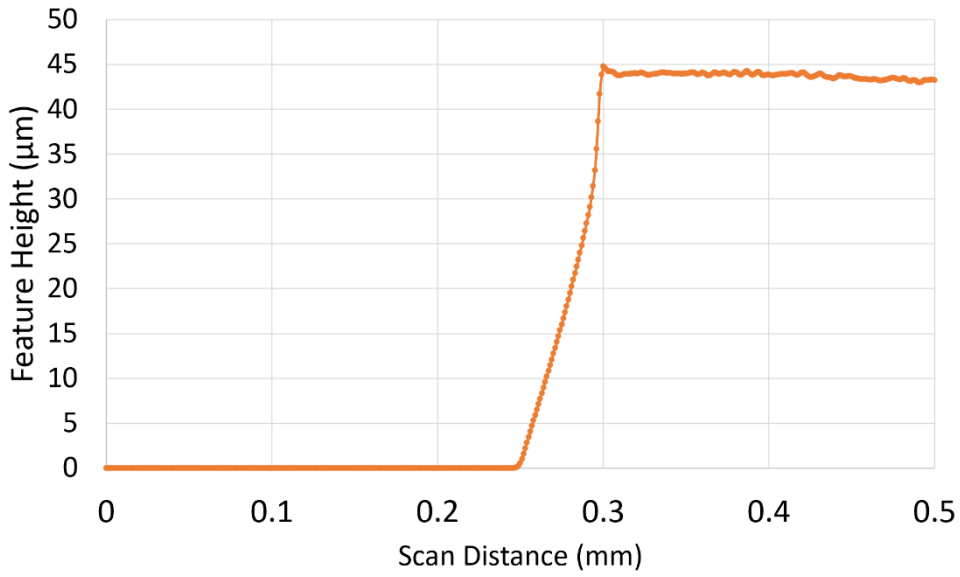

Figure 9. Spin-coating results in the desired thin layer of PDMS for effective Quake valves. The graph shows a sample profilometry profile of PDMS used for our primary channels. Our results demonstrate comparability to previously published data for effective Quake valves [26].

However, decreasing the PDMS thickness made manipulating this layer of PDMS almost impossible. Liftoff and inlet/outlet hole punching frequently resulted in damage to the PDMS, to the extent that most devices were unusable. To remedy this, we decided to spin-coat the same thin layer of PDMS onto the primary channel master but pour a thicker layer of PDMS (on the order of millimeters) onto the valve master. We then performed liftoff and inlet/outlet hole punching on the valve PDMS, aligned the two layers, and plasma bonded the valve PDMS to the primary channel PDMS while the primary channel PDMS was still cured onto its master. Then, we could

use the thicker, valve layer of PDMS as a load-bearing ballast to enable easier liftoff and manipulation of the primary channel PDMS. This method prevented damage to the primary channel layer of PDMS while also facilitating faster fabrication time, ease of manipulation, and robust channel alignment. Figure 8(C-D) shows an overview of this process, while Figure 10 shows the custom alignment tool used to align the two layers. In short, the valve PDMS piece was adhered to a clean glass plate, which was then inverted onto a microscope platform. The primary channel PDMS, still cured onto its master, was placed beneath the glass plate on a moveable microscope stage. The platform with the glass plate was lowered until the valve PDMS piece was just above the primary channel PDMS, so that both pieces were in focus by the microscope. Manual adjustments could be made to the microscope stage x-, y-, and rotational axes to align the two PDMS pieces. Markings were then made for the location of the valve PDMS piece on the glass plate and of the primary channel master on the microscope stage. This was done to facilitate rapid re-alignment of the two layers after exposure to gas plasma, resulting in better bonding. This technique resulted in robust alignment of the two layers, and we recommend this technique for easy manipulation of other thin, PDMS-based microfluidics.

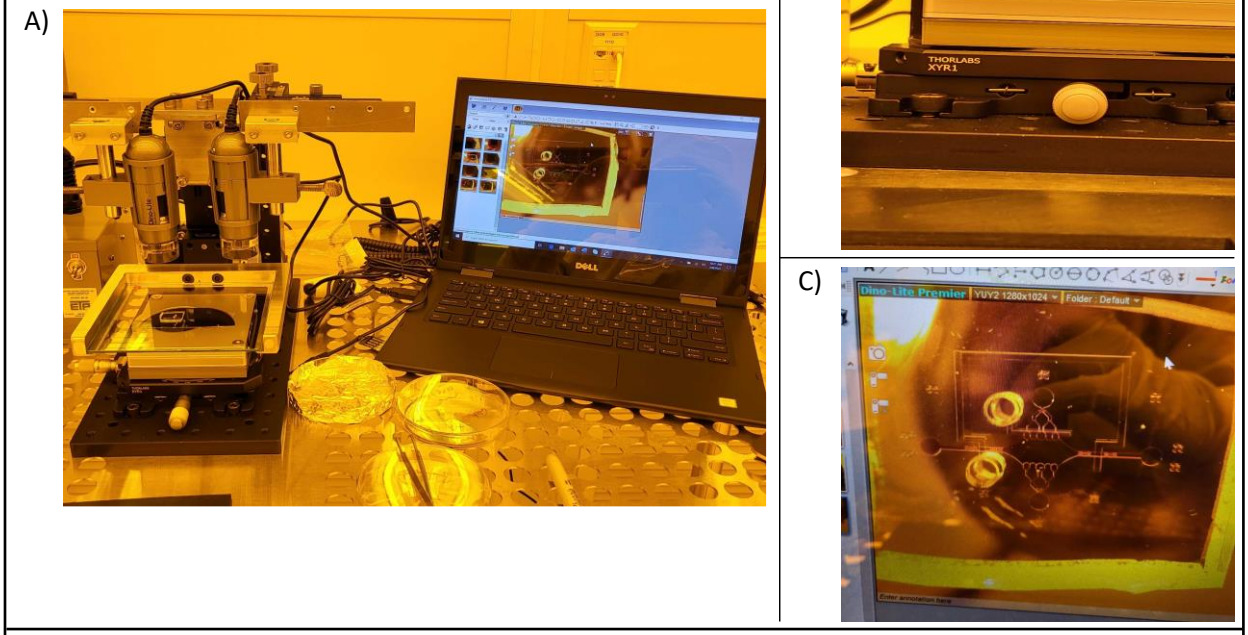

Figure 10. The custom PDMS alignment tool. A) Image of the integrated microscopy tool used to align two layers of PDMS. B) Zoomed-in portion of (A) showing the valve layer PDMS adhered to a glass plate and hanging over the primary channels PDMS, which is still cured onto its master. C) Zoomed-in portion of (A) showing the microscopy software used to assist in proper alignment of the PDMS layers using the rectangular alignment markings around the device periphery. Refer to Appendix A and the Materials and Methods chapter for more information.

3.3.4. Integration with flow control software

Finally, the microfluidic device was integrated with an OB1 flow control system. The OB1 system is used via vendor software and can be programmed to control based on actual flowrate (assuming a corresponding flow sensor is attached in-line) or on system output pressure. The OB1 functions as a pressure-driven controller, using upstream pressure to force fluid from an airtight

source vial through attached tubing. Our system was equipped with two regulating channels, both with a working pressure of 0-200 mbar, and our flow controller had a working range of 0-80 μL/minute. As previously mentioned, the goals of this integration were to reduce the frequency of manual manipulations of the device, such as plugging in and un-plugging tubing, and to provide a more robust flow control than manual pipetting. However, to accommodate multiple reagents flowing into the same inlet port while still preventing cross-contamination, we needed a way to sequester each solution attached to the inlet port. To rectify this, we incorporated a 12-in/1-out in-line bidirectional rotary valve. This distribution valve moderated flow from up to twelve source vials, switching between them so that only one reagent was flown into the microfluidic device at any time. Also, since we only had two regulating channels available on our OB1 system and multiple reagents to flow in, each reagent source vial was simultaneously pressurized from the same OB1 regulating channel using an upstream splitter. Figure 11 shows our integrated setup. Furthermore, while dedicated reagent source vials can be bought from external vendors, we decided to create our own in-house (inlay in Figure 11). By using a standard 1.5 mm biopsy punch, two holes were punched through the lid of a standard 0.6 mL Eppendorf vial. A piece of tubing was attached to each punch hole and Teflon™ tape was used to seal the area around each hole. In one punch hole, one end of the tubing was positioned at the bottom of the vial while the other end connected to the distribution valve. In the other punch hole, one end of the tubing was positioned near the top of the vial while the other end connected to the splitter. In this way, the regulating system could pressurize each reagent source vial simultaneously, but the distribution valve only allowed one reagent at a time to flow into the microfluidic device. Lastly, to prevent air bubbles in the flow lines, each tubing from its reagent source vial was primed prior to connection. It should

be noted that while more OB1 regulating channels can be purchased from the vendor, we used this less expensive splitting technique with good success. Refer to Appendix B for more information.

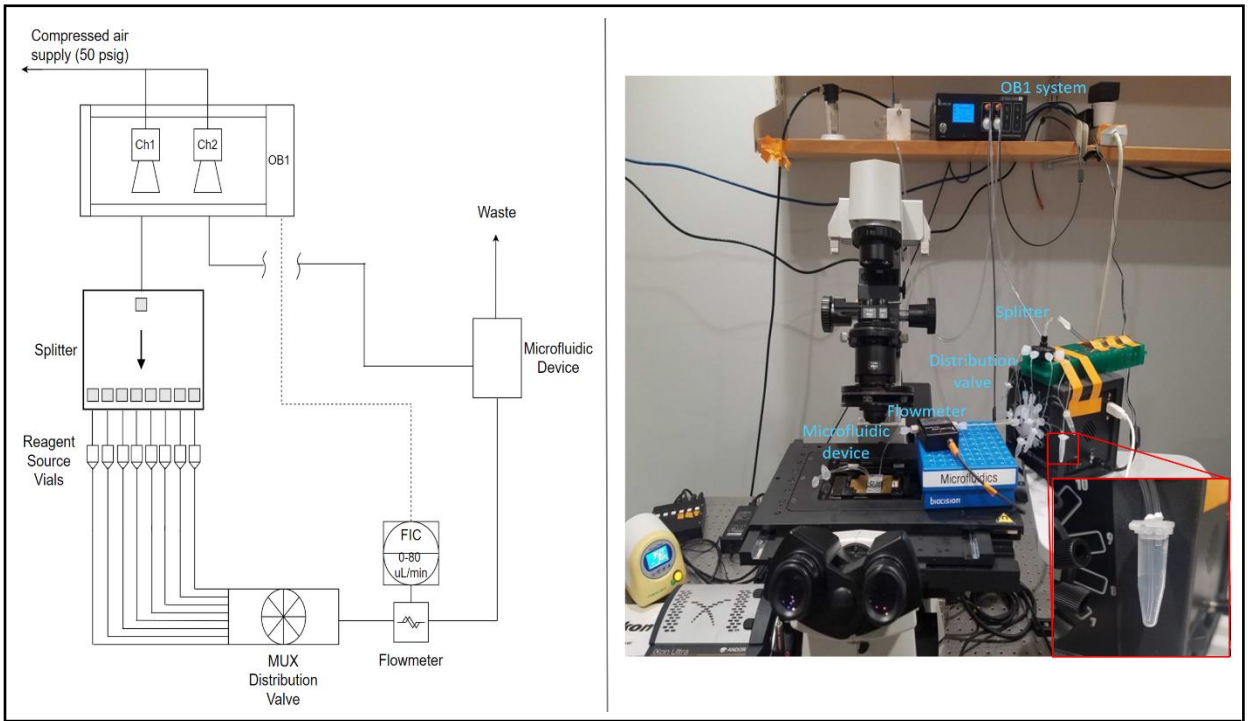

Figure 11. Integration of the microfluidic device with the automated flow controller. Left: Blackbox Piping and Instrumentation Diagram (P&ID) of the integrated system. Right: Annotated image of the setup. Inlay shows zoomed-in image of a reagent source vial created in-house. For more information, refer to Appendix B.

Rather than maintain a constant upstream pressure to generate flow, in many cases we desired to use a flow controller with a feedback loop to maintain a constant flowrate of solution entering the device. However, the pressure and flowrate could be correlated by calibrating the flow controller. Figure 12 shows an example of our calibration to verify the accuracy of the controller flow setpoint as well as determine the pressure setpoint required to achieve each flowrate. This

information could be used to estimate flowrate even if the PID control loop was not utilized and the OB1 system was set to a constant pressure. A manual calibration in this fashion proved helpful when operating at low flowrates, near the limits of the flow controller, when flowrate setpoints resulted in poor flow control. Refer to Appendix B for more information. We also recommend calibrating the flow controller on a regular basis to ensure proper functionality.

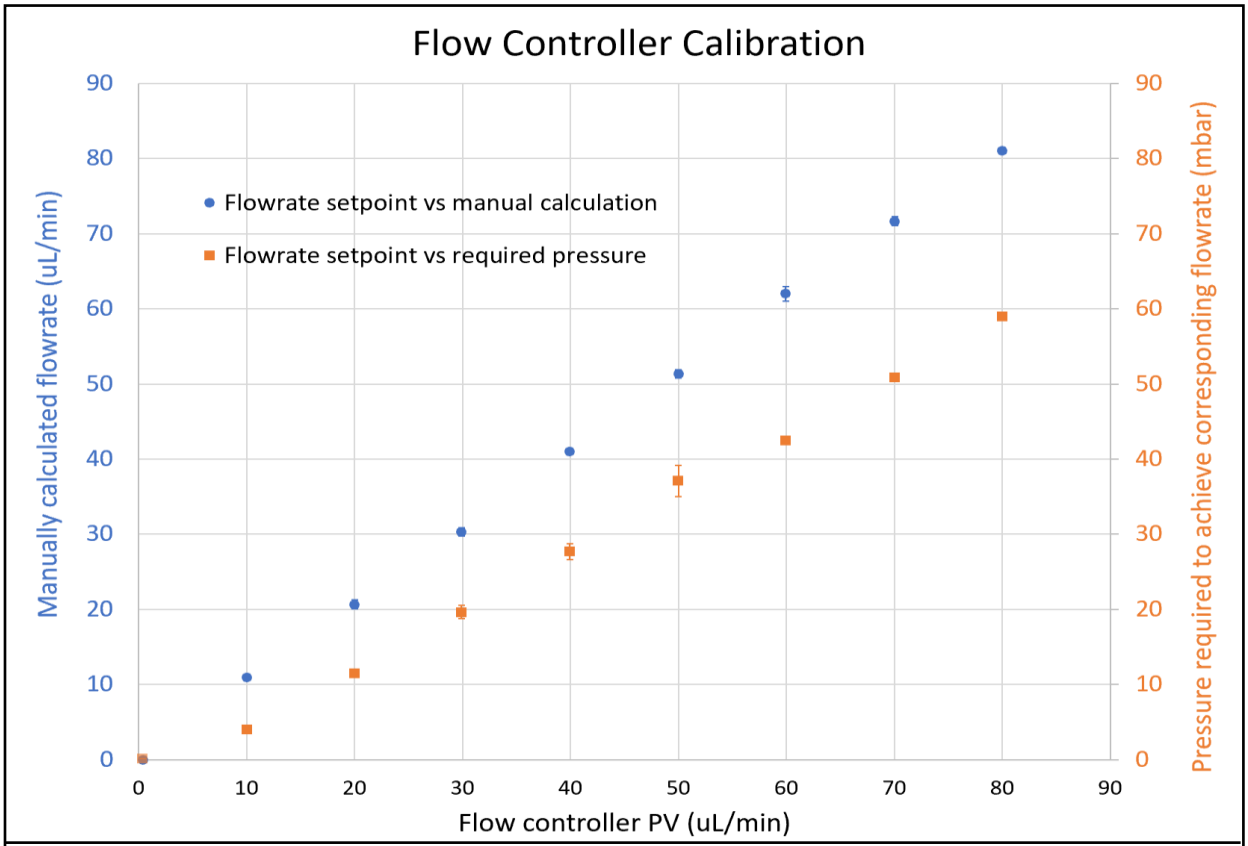

Figure 12. Calibration of flowmeter. The flow controller was set to each setpoint (PV) and allowed to flow for one minute. The pressure required to achieve the flowrate was recorded (right axis), while the volume of solution transferred was manually measured to verify flowrate (left axis). Data points are averages of three trials ran at each setpoint and error bars are standard deviation; error bars are present on each point, but the error may be so small as to be covered by the point itself. For more information, refer to Appendix B.

Finally, the OB1 controller could be coded to automatically control the system. The vendor software affords the ability to program custom recipes, including specifying the desired port for the distribution valve, the desired flowrate and totalized flow volume, and time delays for periods of incubation. Combined with the ability to automate imaging in the microscope software, this system can greatly reduce the amount of manual time spent in preparing, and risk of error in executing, experiments. An image of the user interface (GUI) of the OB1 system is shown in Figure 13.

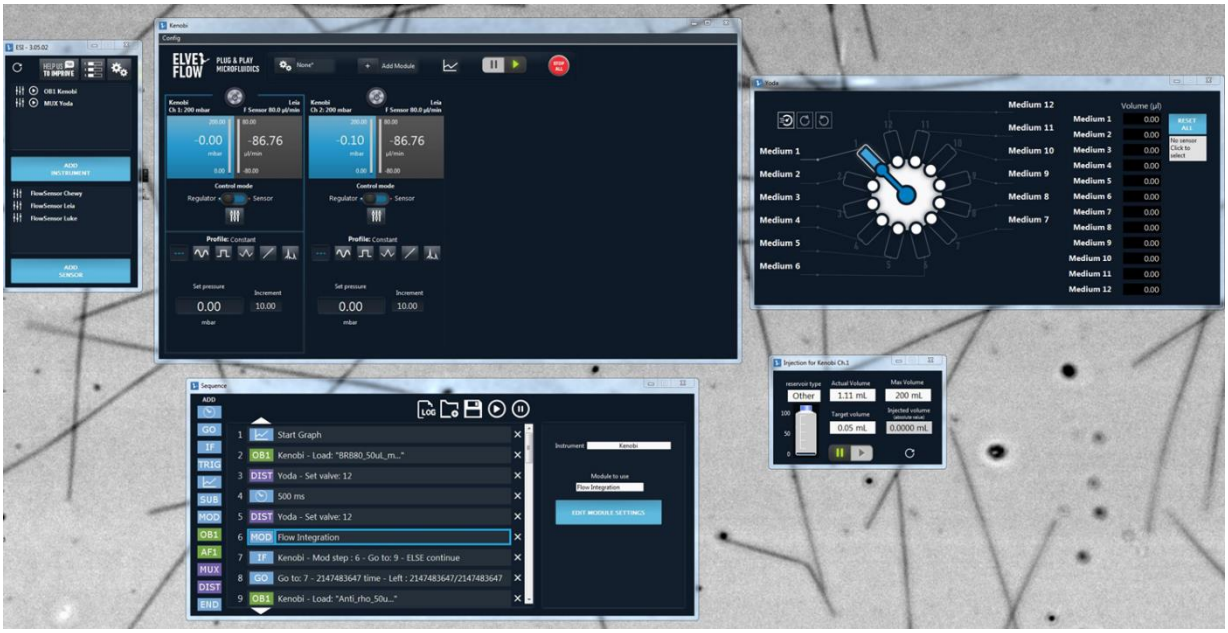

Figure 13. Sample image of the OB1 software GUI. Each regulating channel can be equipped to a flow sensor and independently written pressure/flow control setpoints (top middle). The distribution valve can also be manually rotated (top right). Alternatively, a recipe can be written to automate these parameters for more hands-off experimentation (bottom).

Chapter 4

Results and Discussion, Application to Microtubules

4.1. Microfluidic device preparation and microtubule seeding

Once fabricated, we wanted to use this microfluidic device for investigating microtubule dynamics and biomechanics. The device preparation procedure is detailed in the Materials and Methods chapter and Appendix B. In short, the microfluidic channels were first wetted with BRB80, a standard microtubule buffer solution. The channels were then washed with an anti-rhodamine antibody and incubated for five minutes to coat the 22x22 mm glass coverslip with antibody. Another BRB80 wash was performed to remove the antibody, and the device was then washed and incubated for fifteen minutes with Poloxamer 407. This poloxamer functioned to block the remaining channel surfaces from non-specific protein binding. Another BRB80 wash was performed to remove the poloxamer and prepare for microtubules. Finally, rhodamine labelled, GMPCPP-stabilized microtubule seeds were prepared according to standard protocols and introduced to the device [100,101]. When the desired density of seeds was bound to the coverslip, a BRB80 wash removed excess seeds from solution, and an imaging buffer solution was introduced to the device to prevent photobleaching during imaging.

Interestingly, while we originally created a recipe procedure for the OB1 system to autonomously prepare the microfluidic device and introduce microtubule seeds, this method resulted in poor seed binding to the glass coverslip (Figure 14A). Paradoxically, when performing the same preparation techniques by hand, seed binding worked well (Figure 14B). After discussion with the manufacturer (Saint-Gobain) of the Tygon® tubing used, we believe the most probable

root cause of this discrepancy to be increased residence time of the anti-rhodamine antibody in the tubing when the device was prepared automatically as opposed to when it was prepared by hand. It should be explicitly noted that multiple types of Tygon® tubing exist, and their specific compositions are a trade secret. Per manufacturer discussions, the surface energy of our tubing could be sufficient to induce substantial adsorption of the antibody onto the tubing during fluid transfer. Our troubleshooting seemed to confirm this as a root cause, as the flowrate setpoint of the OB1 automated channel preparation was 50 μL/minute (the maximum achievable flowrate with this flow controller is 80 μL/minute), whereas the manual channel preparation resulted in flow an order of magnitude greater. The difference in residence time of the antibody in the tubing could therefore account for the difference in seed binding. We have been working with the manufacturer to identify a tubing type with less surface energy to facilitate less protein adhesion, in order to use the OB1 system to prepare channels automatically. All experimental results reported below were performed using microfluidic devices that were prepared manually by hand. If the OB1 system was used later in any experiments, it will be noted in the relevant sections.

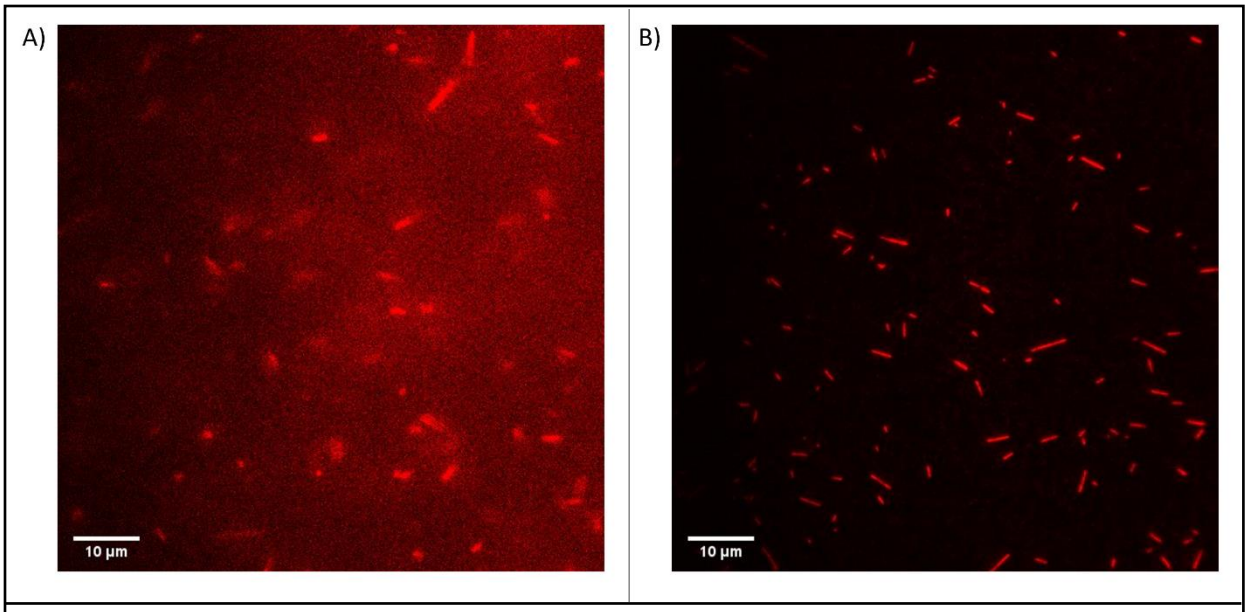

Figure 14. Troubleshooting seed microtubule binding in the microfluidic device. A) Channel prepared automatically using OB1 system resulted in seeds (red) floating in solution but not binding to the coverslip. B) Identical channel preparation done by hand resulted in multiple seeds bound to the coverslip even after the seed solution was washed out of the device. Images are not scaled the same due to high background fluorescence in panel A.

4.2. Microtubule growth and stabilization in device

Once rhodamine-labeled microtubule seeds were bound in the microfluidic device, Alexa Fluor 488-labeled tubulin was introduced to the device and incubated for 15 minutes. Figure 15A shows a sample image during this growth phase. Figure 15B shows two sample kymographs of extensions undergoing dynamic instability during this time. For those unfamiliar with kymographs, the plots are displayed as a 90˚ clockwise rotation of a more traditional time-versus-distance graph. In the kymograph, the vertical axis represents time of the experiment, starting from the top, while the horizontal axis depicts the length of a dynamic microtubule extension(s) from the origin, the microtubule seed. Each horizontal row of pixels represents the state of the

microtubule at a time point, and the rows are stacked together vertically over the entire time to yield the final kymograph. As previously mentioned in the introduction chapter of this thesis, the two microtubule ends have different kinetic rates, with the faster growing end designated as the 'plus' end. This polarity, along with the characteristics of dynamic instability (growth, catastrophe, and rescue) can be seen in the example kymographs of Figure 15B.

After the 15-minute growth period, a 10 μM Taxol® washout was performed to remove any tubulin from solution and stabilize the microtubule extensions that had grown. Taxol has been shown to bind to and stabilize microtubules *in vitro*, but has also been demonstrated to impact microtubule mechanical properties such as flexibility [65,105–107]. Our results reflected these observations; Figure 15C shows the stabilized microtubule extensions more than ten minutes after the initial Taxol® washout, indicating good stability in our system. It should also be noted that microtubules *in vitro* normally grow in a linear manner, as seen in Figure 15A, but the addition of Taxol® results in higher curvature in microtubules [65,105–107].

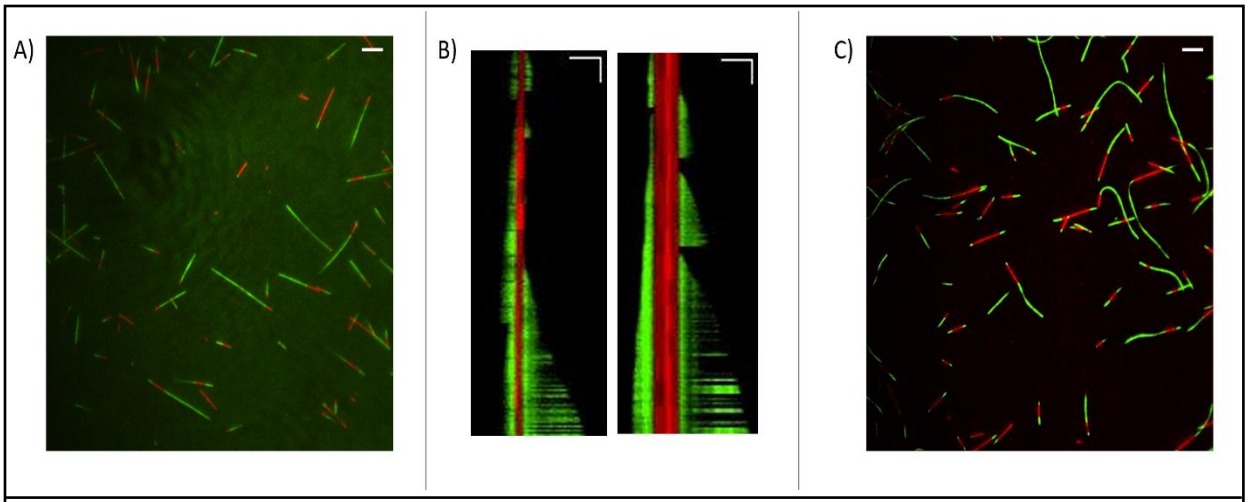

Figure 15. Microtubules can be grown and stabilized using the microfluidic setup. A) Example image of dynamic microtubule extensions (green) growing from seeds (red). The relatively low signal to noise ratio is due to excess Alexa Fluor 488-labeled tubulin in the solution. Scale bar = 5 μm. B) Example kymographs of dynamic microtubules during the 15-minute incubation period. Areas with fluctuating signal, such as near the bottom of the kymographs, indicate that the microtubule extension had moved partially out of the focal plane due to thermal fluctuations. Vertical scale bar = 1 minute, horizontal scale bar = 3 μm. The 488-nm channel (green) was imaged every 5 seconds, the 561-nm channel (red) every minute, and all images were combined to create the kymograph using ImageJ [102,103]. C) Image of Taxol®-stabilized extensions showing higher curvature upon stabilization, compared to the relatively linear profiles in panel A. Scale bar = 5 μm.

4.3. Microtubule bending and flexural rigidity analysis

Once the microtubule extensions were stabilized, they could be bent by flowing solution either manually by hand or using the OB1 control system. The microtubule deflection distance could then be used to estimate flexural rigidity, a metric of the polymer's bending stiffness. Flow

was intended to be perpendicular to the seeding orientation by flowing fluid in the top port of the device and out the bottom port of the device while simultaneously using a Quake valve to block the left and right ports from flow (see Figure 4). When using the OB1 control system to maintain a constant upstream pressure, the local flow experienced by the microtubules could be approximated and used to estimate the microtubules' flexural rigidity.

4.3.1. Derivation of local flow velocity profile

To approximate the local flow experienced by the microtubules, we began with the general Navier-Stokes equation for an incompressible fluid flow:

$$\rho \frac{D\boldsymbol{v}}{Dt} = \rho \boldsymbol{g} - \boldsymbol{\nabla} P + \mu \boldsymbol{\nabla}^2 \boldsymbol{v} \quad (1)$$

Here, ρ is the fluid density; $\frac{D\boldsymbol{v}}{Dt}$ is the substantial derivative of velocity v with respect to time, t; $\boldsymbol{g}$ is the gravitational force; $\boldsymbol{\nabla} P$ is the pressure gradient; and $\mu \boldsymbol{\nabla}^2 \boldsymbol{v}$ is a viscous term with μ as the fluid viscosity.

To solve this equation, we first defined the system by picturing a cross section of the device, as illustrated in Figure 16.

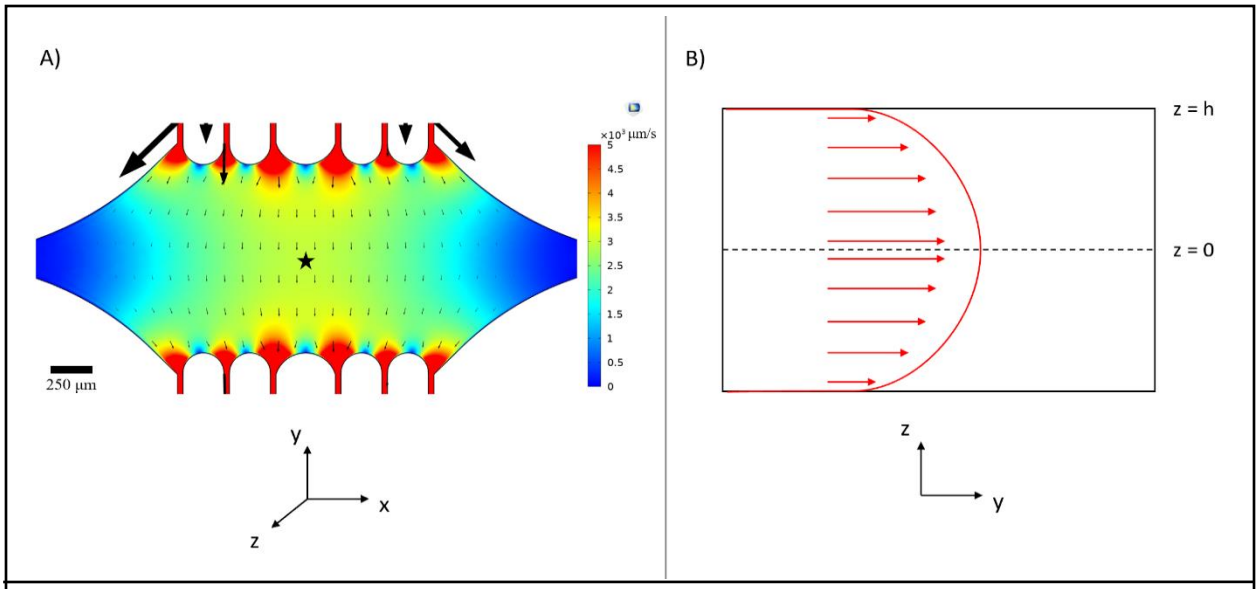

Figure 16. Defining the system for fluid flow analysis of fluid entering the device at the top port and exiting at the bottom port (ports not shown). Left and right ports would be blocked via Quake valve. A) COMSOL simulation of scaled centerline velocity field as in Figure 4B. Star denotes area of interest for panel B. B) Cross-sectional representation of the device. Fully developed fluid flow profile is in the y-direction with a centerline velocity v_c at z = 0 and a no slip boundary condition at the walls. Note that the arrows in this panel are not to scale with respect to the actual velocity field shown in panel A.

In Cartesian coordinates and assuming the flow is one dimensional within the microfluidic device (denoted along the y-axis in our definition of the system), the above equation can be written as:

$$\rho\left(\frac{dv_y}{dt} + v_x\frac{dv_y}{dx} + v_y\frac{dv_y}{dy} + v_z\frac{dv_y}{dz}\right) = -\frac{dP}{dy} + \rho g_y + \mu\left(\frac{d^2v_y}{dx^2} + \frac{d^2v_y}{dy^2} + \frac{d^2v_y}{dz^2}\right) \quad (2)$$

Assuming that the flow is at steady state, laminar, and fully developed, the equation further reduces to the final differential equation:

$$\frac{dP}{dy} = \mu\frac{d^2v_y}{dz^2} \quad (3)$$

For clarity, here μ denotes fluid viscosity. Boundary conditions can be incorporated by assuming no slip at the top or bottom of the device and symmetry at the centerline of the device:

$$v_y = 0 \; at \; z = \pm h \quad (4)$$

$$\frac{dv_y}{dz} = 0 \; at \; z = 0 \quad (5)$$

Solving the differential equation with these two boundary conditions yields the following flow profile:

$$v_y(z) = \frac{z^2}{2\mu}\frac{dP}{dy} - \frac{h^2}{2\mu}\frac{dP}{dy} \quad (6)$$

Reorganization of this solution leads to:

$$v_y(z) = -\frac{1}{2\mu}\frac{dP}{dy}h^2\left(1 - \left(\frac{z}{h}\right)^2\right) \quad (7)$$

The term outside of the parentheses is equivalent to the fluid centerline velocity, v_c, resulting in the final form:

$$v_y(z) = v_c\left(1 - \left(\frac{z}{h}\right)^2\right) \quad (8)$$

The centerline velocity can be simulated in COMSOL, as shown in Figure 16. For a point in the middle of the device experiencing flow driven by an inlet pressure of 50 mbar, the centerline velocity is approximately 3000 μm/second.

However, the microtubules are attached to the glass coverslip, within 100 nm of the surface. Therefore, taking the primary channel master height of 13 μm, as shown in Figure 7, the height of the microtubules can be approximated as z = 6.4 μm. Note that this is because our definition of the system set the z-origin at the center of the device. Solving the equation yields an estimate for the local fluid velocity experienced by the microtubules:

$$v_y(6.4) = 92\frac{\mu m}{second} \quad (9)$$

This velocity can in principle be verified by using fluorescent beads in the bending solution.

4.3.2. Estimating microtubule flexural rigidity using MATLAB

In a seminal 1994 publication, Venier et al. derived an expression to estimate the flexural rigidity of a microtubule extension [108]. The final form of their equation, the derivation of which is described elsewhere, is [108]:

$$y = \frac{\pi\eta V L^4}{6K \ln\left(\frac{L}{2d}\right)}\left[\left(\frac{x}{L}\right)^4 - 4\left(\frac{x}{L}\right)^3 + 6\left(\frac{x}{L}\right)^2\right] \quad (10)$$

Here, those authors have defined η as the fluid viscosity, V as the velocity experienced by the microtubule, L as the total microtubule extension length, d as the microtubule diameter, K as the flexural rigidity, x as a manually defined distance along the microtubule length L, and y as the amount of deflection from baseline that the associated point x underwent when subjected to flow. Multiple (x, y) pairs were gathered and plotted to yield a bending curve of the actual microtubule. Sample curves were then generated by iteratively modifying the value of K in the equation (since all other variables were known), and the sample curve which best matched the actual bending profile of the microtubule yielded an approximation of the actual microtubule's flexural rigidity.

We adopted the same approach by writing a custom MATLAB script for this equation, but with a slight modification to account for the orientation of the microtubule relative to the flow vector (refer to Appendix C for the MATLAB script). While ideally the microtubule extension would be perpendicular to the direction of flow in our system, the microtubule seed may not perfectly align in this orientation, potentially due to friction factors as the seeds stratified out of solution and bound to the antibody-coated coverslip. A geometric term was therefore added to the equation to compensate for θ, the orientation angle relative to flow:

$$y = \sin\theta * \frac{\pi\eta V L^4}{6K \ln\left(\frac{L}{2d}\right)}\left[\left(\frac{x}{L}\right)^4 - 4\left(\frac{x}{L}\right)^3 + 6\left(\frac{x}{L}\right)^2\right] \quad (11)$$

At orthogonal angles, the modified equation reduces to the original equation. For each microtubule analyzed, the microtubule's extension length, L, and its orientation with respect to flow, θ, were calculated using ImageJ; the fluid viscosity, η, was assumed to be that of water, the primary solvent used in our applications; and the diameter of a typical microtubule lattice was taken to be 25 nanometers [109–111]. To determine x-values for each microtubule, positions along the microtubule length were manually defined while the microtubule was at rest. Then, the distance that each point was deflected upon bending was manually measured to yield a corresponding y-value. Of note, due to the Taxol®-induced curvature of some of the microtubule extensions, only microtubules that remained relatively straight after the Taxol® washout were selected for this analysis. An example image of microtubules in a resting state and when bent is shown in Figure 17.

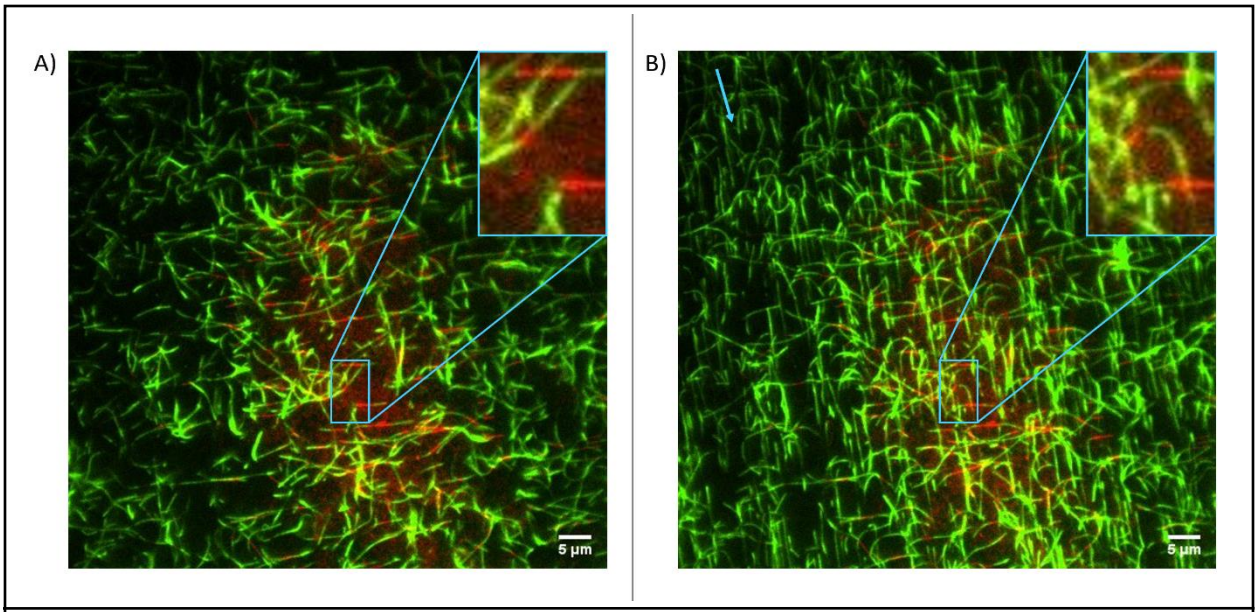

Figure 17. The microfluidic setup can be used to bend stabilized microtubules. A) Microtubules in a resting state after stabilization with Taxol®. B) Microtubules bending under flow generated by an OB1-controlled constant upstream pressure of 50 mbar (arrow denotes direction of flow). Inlay in each image shows an enlargement of an example microtubule selected for analysis.

While the purpose of this thesis was to demonstrate a proof-of-concept for using our microfluidic device for investigating microtubule properties, this analysis precipitates a discussion on limitations and areas for improvement. First, due to the relatively high seed density in the field of view and the long microtubule extensions, it was difficult to identify microtubules fit for analysis (see Figure 17). Microtubule extensions that crossed over other extensions could have their bending profiles impacted by this interaction, and the considerable number of microtubules in a field of view made it difficult to manually track a single extension's bending profile. Reducing the number of seeds attached to the coverslip, such as by automating the device preparation (once an appropriate tubing is identified), will help reduce this uncertainty and increase the sample size. Second, we also acknowledge that manually defining the positions along the microtubule and

measuring their deflected distances can be subject to error. The development of an automated code that identifies the positions along the microtubule and their respective deflection distances upon bending would improve the robustness of this method.

Regardless of these limitations, in the few microtubules analyzed, we determined that the flexural rigidity of the Taxol-stabilized microtubules in our system was $3.2 \pm 2.5 \times 10^{-24}$ N*m^2 (average ± standard deviation, n = 3). Figure 18 shows the MATLAB output graph for estimating the flexural rigidity of the microtubule outlined in Figure 17. While our sample size was low, this flexural rigidity estimate aligns well with previously published studies, which reported flexural rigidity values within the regime of 10^{-24} - 10^{-23} N*m^2; for example, the average flexural rigidity of paclitaxel-stabilized microtubules was reported as 2.0×10^{-24} N*m^2 from Kikumoto, *et al*., and 4.7×10^{-24} N*m^2 from Venier, *et al*. [105,108,112,113]. This suggests that our microfluidic system can be used in combination with COMSOL and MATLAB analyses to further investigate microtubule flexural rigidity under a variety of conditions.

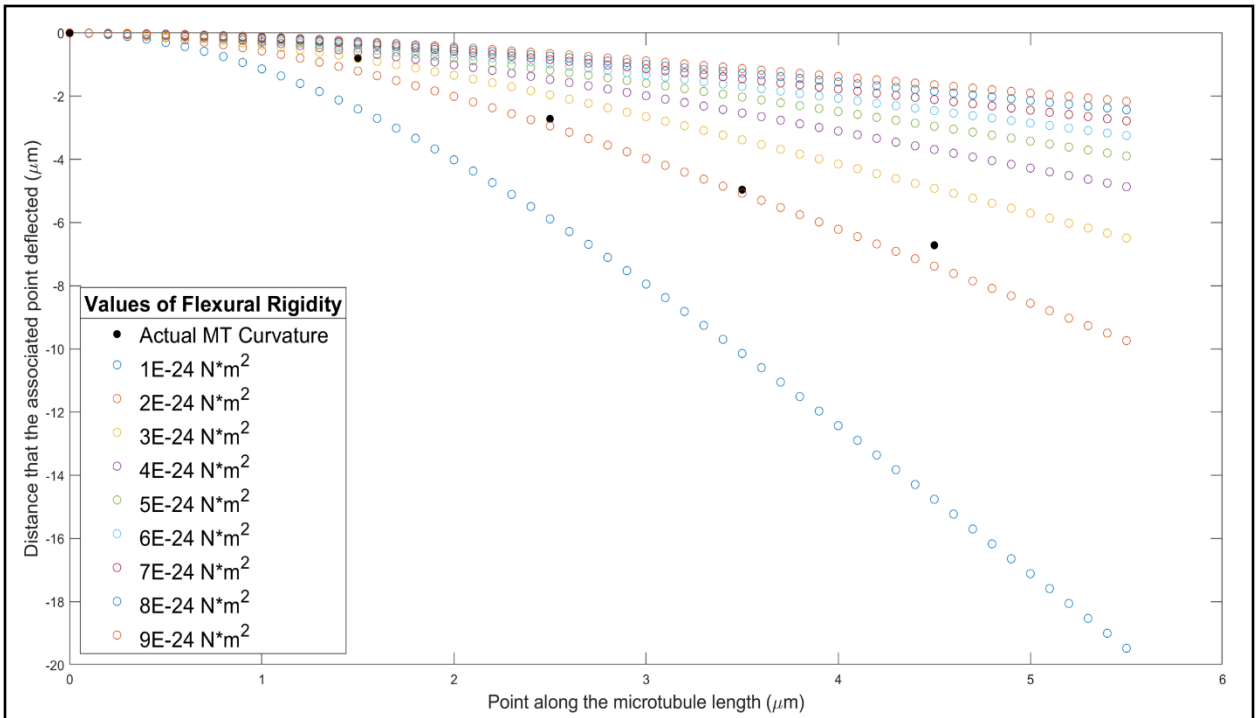

Figure 18. MATLAB can accurately estimate microtubule flexural rigidity from bending data. This simulation was used to estimate the flexural rigidity of the bending microtubule specified in Figure 17B. The actual microtubule was approximately 5.5 micrometers long and oriented approximately 90˚ with respect to flow. The manually traced, actual bending profile is shown in solid black dots. Colored circles indicate bending profiles according to Equation (11), assuming varying values of flexural rigidity. From this data, the microtubule's flexural rigidity was approximated to be 2 x 10^{-24} N*m^2, which agrees well with other reported values [105,108,112,113].

Chapter 5

Conclusions and Future Directions

The primary goal of this thesis was to design and fabricate a two-layered microfluidic device that could be used to investigate microtubule dynamics and mechanics *in vitro*. The design basis was precipitated by our desire to utilize the intrinsic benefits of PDMS-based microfluidic devices while also prototyping a combination of features to enable robust, customizable, and high-throughput experimentation.

This goal has been successfully achieved through several modalities. By using a strategy of multi-layer alignment, we were able to create diaphragm-like valves to sequester fluid within certain areas of the device. A resist reflow technique further improved these valve systems by creating rounded channel features. The inclusion of redundant bubble traps also decreases the likelihood of protein denaturation due to air bubbles in the microfluidic device. Finally, the integration of the microfluidic device with an automated flow control software affords a wide degree of experimental customization while saving time and resources, and reducing the possibility of manual error. For example, multiple conditions can be run simultaneously in a single device, either by establishing gradients of solutions or sequestering certain areas from flow. Further, incorporating a rotary distribution valve with the flow control system increases the number of reagents available to the device in a single setup by an order of magnitude, allowing for more complex experimentation. This distribution valve, alongside the reagent source vials we created in-house, is estimated to save thousands of dollars that otherwise would be spent on hardware upgrades to achieve the same experimental degrees of freedom. Fabrication protocols and general

guidelines were also generated to facilitate smooth technology transfer and serve as a basis for future users of this system. Demonstration of our device's operability was shown by preparing the device system, then growing, stabilizing, and bending microtubule extensions in the device using either manual or automatic, controller-regulated flow. Aided by COMSOL modeling and MATLAB analysis, biomechanical properties of microtubules, such as flexural rigidity, were also probed using our system.

There is, however, still room for improvement. As mentioned in previous chapters, there are three areas of particular interest that, if rectified, would facilitate a more robust system and associated experimental analysis. First, we discovered that our current type of Tygon® tubing was likely inhibiting the anti-rhodamine antibody from reaching the device when the antibody was flown in using the automated control system. We suspect that the antibody adhered to the relatively active surface of the tubing during its residence time in the tubing, leaving little of the microfluidic channel coated in antibody and thus preventing the binding of microtubule seeds within the channel. While we engineered a workaround for this problem (flowing the anti-rhodamine solution by hand reduced the residence time and allowed antibody coating of the channel), it is more desirable to automate the entire sequence of solutions introduced to the device. Fully automating the system reduces the chance for manual error and saves the researcher time. A different tubing type may help with this problem. Second, we found that on average, the microtubule seeding density in the device was too large to reliably measure extension length and bending profiles. The potential for extensions to interact with each other, or the overlap of signal from multiple microtubules in proximity, made manual measurements difficult and reduced the quantity of microtubules available for analysis. Reducing the time seeds are allowed to bind in the device, such as by automating the BRB80 washout using the OB1 controller and distribution valve, or

fine-tuning the time allowed for extension growth under different concentrations of tubulin could help with this issue. Furthermore, the seeds would not always be oriented directly along the x-axis of the device as desired. This could be due to friction forces as the seeds began to bind to the coverslip, or large shear stresses on the seeds breaking the seeds into smaller components that were then less prone to align with the flow. Future optimizations to create longer seeds or flow profiles with lower shear stress may help rectify this issue. Third is the related opportunity of improving flexural rigidity estimation using computational analysis. Rather than manually defining points along the microtubule lattice and measuring the amount of deflection those points undergo during bending, an automated code would greatly reduce the time required for analysis and lead to more precise results. Automating the calculation of multiple microtubules' deflection profiles would standardize the way measurements are made and generate more robust and efficient analyses.

While there is still room for improvement, our microfluidic device and integrated systems show promise. Our advancements allow for a range of experimental setups which enable more robust, high-thoughput testing capabilities than previous assays. Furthermore, experiments can be automated using flow controllers and the distribution valve to reduce load on the researcher while maintaining precise flow profiles or concentration gradients in the device. Some potential future applications of this setup include investigating the effect of microtubule-associated proteins (MAPs) on microtubule flexural rigidity, the effect of MAPs on microtubule dynamics and lattice damage/repair, and the biomechanical interactions of microtubules and actin filaments. The synthesis of microfabrication, automated recipe control, and computational modeling and analysis techniques enables a flexible system fit for probing the cellular cytoskeleton *in vitro*.

References

1. Whitesides, G. M. The origins and the future of microfluidics. *Nature* **442**, 368–373 (2006).
2. Dellaquila, A. Five Short Stories on The History of Microfluidics. https://www.elveflow.com/microfluidic-reviews/general-microfluidics/history-of-microfluidics/.
3. Choi, H. & Mody, C. C. M. The long history of molecular electronics: Microelectronics origins of nanotechnology. *Soc. Stud. Sci.* **39**, 11–50 (2009).
4. Heather, J. M. & Chain, B. The sequence of sequencers: The history of sequencing DNA. *Genomics* **107**, 1–8 (2016).
5. Terry, S. C., Herman, J. H. & Angell, J. B. A Gas Chromatographic Air Analyzer Fabricated on a Silicon Wafer. *IEEE Trans. Electron Devices* **26**, 1880–1886 (1979).
6. Wang, J. Microchip devices for detecting terrorist weapons. *Anal. Chim. Acta* **507**, 3–10 (2004).
7. Whitesides, G. M. & Stroock, A. D. Flexible methods for microfluidics. *Phys. Today* **54**, 42 (2001).
8. Duffy, D. C., McDonald, J. C., Schueller, O. J. A. & Whitesides, G. M. Rapid prototyping of microfluidic systems in poly(dimethylsiloxane). *Anal. Chem.* **70**, 4974–4984 (1998).
9. Dittrich, P. S. & Manz, A. Lab-on-a-chip: Microfluidics in drug discovery. *Nat. Rev. Drug Discov.* **5**, 210–218 (2006).
10. Neužil, P., Giselbrecht, S., Länge, K., Huang, T. J. & Manz, A. Revisiting lab-on-a-chip technology for drug discovery. *Nat. Rev. Drug Discov.* **11**, 620–632 (2012).

11. Manz, A., Graber, N. & Widmer, H. M. Miniaturized Total Chemical Analysis Systems: a Novel Concept for Chemical Sensing. *Sensors and Actuators* 244–248 (1990).

12. Harrison, D. J. *et al.* Micromachining a miniaturized capillary electrophoresis-based chemical analysis system on a chip. *Science (80-.).* **261**, 895–897 (1993).

13. Knight, J. Microfluidics: Honey, I shrunk the lab. *Nature* **418**, 474+ (2002).

14. Squires, T. M. & Quake, S. R. Microfluidics: Fluid physics at the nanoliter scale. *Rev. Mod. Phys.* **77**, (2005).

15. Beebe, D. J., Mensing, G. A. & Walker, G. M. Physics and applications of microfluidics in biology. *Annu. Rev. Biomed. Eng.* **4**, 261–286 (2002).

16. Ng, J. M. K., Stroock, A. D. & Whitesides, G. M. Components for integrated poly (dimethylsiloxane) microfluidic systems. 3461–3473 (2010).

17. Nall, J. R. & Lathrop, J. W. Photolithographic fabrication techniques for transistors which are an integral part of a printed circuit. in *1957 International Electron Devices Meeting* 117 (1957). doi:10.1109/IEDM.1957.187078.

18. Lathrop, J. W. & Nall, J. R. Semiconductor Construction. *U.S. Pat. 2890395* 8 (1959).

19. Rogers, J. A., Paul, K. E., Jackman, R. J. & Whitesides, G. M. Using an elastomeric phase mask for sub-100 nm photolithography in the optical near field. *Appl. Phys. Lett.* **70**, 2658–2660 (1997).

20. Wu, Y. A., Panigrahi, B., Lu, Y. H. & Chen, C. Y. An Integrated Artificial Cilia Based Microfluidic Device for Micropumping and Micromixing Applications. *Micromachines* **8**, 1–11 (2017).

21. Tanyeri, M., Ranka, M., Sittipolkul, N. & Schroeder, C. M. A microfluidic-based hydrodynamic trap: Design and implementation. *Lab Chip* **11**, 1786–1794 (2011).

22. Lemke, E. A. *et al.* Microfluidic device for single-molecule experiments with enhanced photostability. *J. Am. Chem. Soc.* **131**, 13610–13612 (2009).

23. Mohan, R. *et al.* Design considerations for elastomeric normally closed microfluidic valves. *Sensors Actuators, B Chem.* **160**, 1216–1223 (2011).

24. Cambier, T. *et al.* Design of a 2D no-flow chamber to monitor hematopoietic stem cells. *Lab Chip* **15**, 77–85 (2015).

25. Fordyce, P. M., Diaz-Botia, C. A., Derisi, J. L. & Gomez-Sjoberg, R. Systematic characterization of feature dimensions and closing pressures for microfluidic valves produced via photoresist reflow. *Lab Chip* **12**, 4287–4295 (2012).

26. Unger, M. A., Chou, H. P., Thorsen, T., Scherer, A. & Quake, S. R. Monolithic microfabricated valves and pumps by multilayer soft lithography. *Science (80-.).* **288**, 113–116 (2000).

27. Cheng, D. & Jiang, H. A debubbler for microfluidics utilizing air-liquid interfaces. *Appl. Phys. Lett.* **95**, 1–4 (2009).

28. Voldman, J., Member, S., Gray, M. L. & Schmidt, M. A. An Integrated Liquid Mixer / Valve. **9**, 295–302 (2000).

29. Whitesides, G. M., Ostuni, E., Jiang, X. & Ingber, D. E. Soft Lithography in Biology and Biochemistry. *Annu. Rev. Biomed. Eng.* **3**, 335–73 (2001).

30. Frank, P., Haefner, S., Paschew, G. & Richter, A. Rounding of negative dry film resist by diffusive backside exposure creating rounded channels for pneumatic membrane valves. *Micromachines* **6**, 1588–1596 (2015).

31. Lee, J. B., Choi, K. H. & Yoo, K. Innovative SU-8 lithography techniques and their applications. *Micromachines* **6**, 1–18 (2015).

32. Kim, P. *et al.* Soft lithography for microfluidics: A Review. *Biochip J.* **2**, 1–11 (2008).

33. Venkatesan, S., Jerald, J., Asokan, P. & Prabakaran, R. A Comprehensive Review on Microfluidics Technology and its Applications. in *Recent Advances in Mechanical Engineering* (eds. Kumar, H. & Jain, P. K.) 235–245 (Springer Singapore, 2020).

34. Minteer, S. *Microfluidic Techniques: Reviews and Protocols*. (2006).

35. Mitra, S. K. & Chakraborty, S. *Microfluidics and nanofluidics handbook: Fabrication, implementation, and applications*. *Microfluidics and Nanofluidics Handbook: Fabrication, Implementation, and Applications* (2016).

36. Ng Lee, J., Park, C. & Whitesides, G. M. Solvent Compatibility of Poly(dimethylsiloxane)-Based Microfluidic Devices. (2003).

37. Liu, X. *et al.* High-throughput screening of antibiotic-resistant bacteria in picodroplets. *Lab Chip* **16**, 1636–1643 (2016).

38. Sackmann, E. K., Fulton, A. L. & Beebe, D. J. The present and future role of microfluidics in biomedical research. *Nature* **507**, 181–189 (2014).

39. Erickson, D. & Li, D. Integrated microfluidic devices. *Anal. Chim. Acta* **507**, 11–26 (2004).

40. Shepherd, R. F. *et al.* Using explosions to power a soft robot. *Angew. Chemie - Int. Ed.* **52**, 2892–2896 (2013).

41. Shepherd, R. F. *et al.* Multigait soft robot. *Proc. Natl. Acad. Sci. U. S. A.* **108**, 20400–20403 (2011).

42. Wehner, M. *et al.* An integrated design and fabrication strategy for entirely soft, autonomous robots. *Nature* **536**, 451–455 (2016).

43. Iliescu, C. Microfluidics in glass: Technologies and applications. *Inf. Midem -Ljubljana-*

36, 204–211 (2006).

44. Shah, R. K. *et al.* Designer emulsions using microfluidics. *Mater. Today* **11**, 18–27 (2008).

45. Othman, R., Vladisavljević, G. T. & Nagy, Z. K. Preparation of biodegradable polymeric nanoparticles for pharmaceutical applications using glass capillary microfluidics. *Chem. Eng. Sci.* **137**, 119–130 (2015).

46. Chen, Y., Gao, W., Zhang, C. & Zhao, Y. Three-dimensional splitting microfluidics. *Lab Chip* **16**, 1332–1339 (2016).

47. Li, X., Ballerini, D. R. & Shen, W. A perspective on paper-based microfluidics: Current status and future trends. *Biomicrofluidics* **6**, (2012).

48. Park, T. S., Li, W., McCracken, K. E. & Yoon, J. Y. Smartphone quantifies Salmonella from paper microfluidics. *Lab Chip* **13**, 4832–4840 (2013).

49. Dungchai, W., Chailapakul, O. & Henry, C. S. Electrochemical detection for paper-based microfluidics. *Anal. Chem.* **81**, 5821–5826 (2009).

50. Yetisen, A. K., Akram, M. S. & Lowe, C. R. Paper-based microfluidic point-of-care diagnostic devices. *Lab Chip* **13**, 2210–2251 (2013).

51. Hu, J. *et al.* Advances in paper-based point-of-care diagnostics. *Biosens. Bioelectron.* **54**, 585–597 (2014).

52. Volpatti, L. R. & Yetisen, A. K. Commercialization of microfluidic devices. *Trends Biotechnol.* **32**, 347–350 (2014).

53. Grand View Research Inc. *Microfluidics Market Size, Industry Report, 2021-2028*. https://www.grandviewresearch.com/industry-analysis/microfluidics-market (2021).

54. MarketsandMarkets. Microfluidics Market. https://www.marketsandmarkets.com/Market-

Reports/microfluidics-market-1305.html.

55. Rogers, M. *et al.* Engineered microfluidic bioreactor for examining the three-dimensional breast tumor microenvironment. *Biomicrofluidics* **12**, 1–12 (2018).

56. Huh, D. *et al.* Reconstituting Organ-Level Lung Functions on a Chip. *Science (80-.).* **328**, 1662 LP – 1668 (2010).

57. Tung, C. K. *et al.* Microgrooves and fluid flows provide preferential passageways for sperm over pathogen Tritrichomonas foetus. *Proc. Natl. Acad. Sci. U. S. A.* **112**, 5431–5436 (2015).

58. Lin, C. T., Kao, M. T., Kurabayashi, K. & Meyhofer, E. Self-contained, biomolecular motor-driven protein sorting and concentrating in an ultrasensitive microfluidic chip. *Nano Lett.* **8**, 1041–1046 (2008).

59. Aoun, L. *et al.* Microdevice arrays of high aspect ratio poly(dimethylsiloxane) pillars for the investigation of multicellular tumour spheroid mechanical properties. *Lab Chip* **14**, 2344–2353 (2014).

60. Alberts, B. *et al. Molecular Biology of the Cell*. (W. W. Norton & Company, 2014).

61. Howard, J. *Mechanics of motor proteins and the cytoskeleton*. (Sinauer Associates, Inc., 2001). doi:10.1063/1.1472396.

62. McIntosh, J. R. & Landis, S. C. The distribution of spindle microtubules during mitosis in cultured human cells. *J. Cell Biol.* **49**, 468–497 (1971).

63. Vulevic, B. & Correia, J. J. Thermodynamic and structural analysis of microtubule assembly: The role of GTP hydrolysis. *Biophys. J.* **72**, 1357–1375 (1997).

64. Xiao, H. *et al.* Insights into the mechanism of microtubule stabilization by Taxol. *Proc. Natl. Acad. Sci. U. S. A.* **103**, 10166–10173 (2006).

65. Yang, C. P. H. & Horwitz, S. B. Taxol®: The first microtubule stabilizing agent. *Int. J. Mol. Sci.* **18**, (2017).

66. Yvon, A. M. C., Wadsworth, P. & Jordan, M. A. Taxol suppresses dynamics of individual microtubules in living human tumor cells. *Mol. Biol. Cell* **10**, 947–959 (1999).

67. Matamoros, A. J. & Baas, P. W. Microtubules in health and degenerative disease of the nervous system. *Brain Res. Bull.* **126**, 217–225 (2016).

68. Baird, F. J. Microtubule Defects and Neurodegeneration. *J. Genet. Syndr. Gene Ther.* **04**, 1–14 (2013).

69. Matsuyama, S. S. & Jarvik, L. F. Hypothesis: Microtubules, a key to Alzheimer disease. *Proc. Natl. Acad. Sci. U. S. A.* **86**, 8152–8156 (1989).

70. Del C. Alonso, A. *et al.* Interaction of Tau Isoforms with Alzheimer's Disease Abnormally Hyperphosphorylated Tau and in Vitro Phosphorylation into the Disease-like Protein. *J. Biol. Chem.* **276**, 37967–37973 (2001).

71. Carlier, M. F. & Pantaloni, D. Kinetic Analysis of Guanosine 5'-Triphosphate Hydrolysis Associated with Tubulin Polymerization. *Biochemistry* **20**, 1918–1924 (1981).

72. Roostalu, J. *et al.* The speed of GTP hydrolysis determines GTP cap size and controls microtubule stability. *Elife* **9**, 1–22 (2020).

73. Chaaban, S. & Brouhard, G. J. A microtubule bestiary: Structural diversity in tubulin polymers. *Mol. Biol. Cell* **28**, 2924–2931 (2017).

74. Mitchison, T. & Kirschner, M. Dynamic instability of microtubule growth. *Nature* **312**, 237–242 (1984).

75. Endow, S. A., Kull, F. J. & Liu, H. Kinesins at a glance. *J. Cell Sci.* **123**, 3420–3424 (2010).

76. Brouhard, G. J. & Rice, L. M. Microtubule dynamics: An interplay of biochemistry and mechanics. *Nat. Rev. Mol. Cell Biol.* **19**, 451–463 (2018).

77. Schaedel, L. *et al.* Microtubules self-repair in response to mechanical stress. *Nat. Mater.* **14**, 1156–1163 (2015).

78. Chu, S. H. *et al.* A microfluidic device for in situ fixation and super-resolved mechanosensation studies of primary cilia. *Biomicrofluidics* **13**, (2019).

79. Geisterfer, Z. M., Zhu, D. Y., Mitchison, T. J., Oakey, J. & Gatlin, J. C. Microtubule Growth Rates Are Sensitive to Global and Local Changes in Microtubule Plus-End Density. *Curr. Biol.* **30**, 3016-3023.e3 (2020).

80. Schaedel, L. *et al.* Lattice defects induce microtubule self-renewal. *Nat. Phys.* **15**, 830–838 (2019).

81. Aher, A. *et al.* CLASP Mediates Microtubule Repair by Restricting Lattice Damage and Regulating Tubulin Incorporation. *Curr. Biol.* **30**, 2175-2183.e6 (2020).

82. Duellberg, C., Cade, N. I., Holmes, D. & Surrey, T. The size of the EB cap determines instantaneous microtubule stability. *Elife* **5**, (2016).

83. Fourniol, F. J. *et al. Micropattern-guided assembly of overlapping pairs of dynamic microtubules*. *Methods in Enzymology* vol. 540 (Elsevier Inc., 2014).

84. Vleugel, M., Roth, S., Groenendijk, C. F. & Dogterom, M. Reconstitution of basic mitotic spindles in spherical emulsion droplets. *J. Vis. Exp.* **2016**, (2016).

85. Duellberg, C., Cade, N. I. & Surrey, T. Microtubule aging probed by microfluidics-Assisted tubulin washout. *Mol. Biol. Cell* **27**, 3563–3573 (2016).

86. VanDelinder, V., Brener, S. & Bachand, G. D. Mechanisms Underlying the Active Self-Assembly of Microtubule Rings and Spools. *Biomacromolecules* **17**, 1048–1056 (2016).

87. Roth, S., Gârlea, I. C., Vleugel, M., Mulder, B. M. & Dogterom, M. Reconstitution of basic mitotic spindles in cell-like confinement. *bioRxiv* (2019) doi:10.1101/770602.

88. Xu, Z. *et al.* Microtubules acquire resistance from mechanical breakage through intralumenal acetylation. *Science (80-.).* **356**, 328–332 (2017).

89. Fanalista, F. *et al.* Shape and Size Control of Artificial Cells for Bottom-Up Biology. *ACS Nano* **13**, 5439–5450 (2019).

90. Velve-Casquillas, G., Costa, J., Carlier-Grynkorn, F., Mayeux, A. & Tran, P. T. A Fast Microfluidic Temperature Control Device for Studying Microtubule Dynamics in Fission Yeast. *Methods Cell Biol.* **97**, 185–201 (2010).

91. Portran, D., Schaedel, L., Xu, Z., Théry, M. & Nachury, M. V. Tubulin acetylation protects long-lived microtubules against mechanical ageing. *Nat. Cell Biol.* **19**, 391–398 (2017).

92. Huang, Y. M., Uppalapati, M., Hancock, W. O. & Jackson, T. N. Microtubule transport, concentration and alignment in enclosed microfluidic channels. *Biomed. Microdevices* **9**, 175–184 (2007).

93. Uppalapati, M., Huang, Y., Shastry, S., Jackson, T. N. & Hancock, W. O. Microtubule motors in microfluidics. *Methods Bioeng. Microfabr. Microfluid.* 311–337 (2009).

94. Sung, J. H. & Shuler, M. L. Prevention of air bubble formation in a microfluidic perfusion cell culture system using a microscale bubble trap. *Biomed. Microdevices* **11**, 731–738 (2009).

95. Williams, M. J. *et al.* A Low-Cost, Rapidly Integrated Debubbler (RID) Module for Microfluidic Cell Culture Applications. *Micromachines* vol. 10 (2019).

96. Nakayama, T. *et al.* Circumventing air bubbles in microfluidic systems and quantitative

continuous-flow PCR applications. *Anal. Bioanal. Chem.* **386**, 1327–1333 (2006).

97. Park, S., Cho, H., Kim, J. & Han, K.-H. Lateral Degassing Method for Disposable Film-Chip Microfluidic Devices. *Membranes* vol. 11 (2021).

98. Pereiro, I., Fomitcheva Khartchenko, A., Petrini, L. & Kaigala, G. V. Nip the bubble in the bud: A guide to avoid gas nucleation in microfluidics. *Lab Chip* **19**, 2296–2314 (2019).

99. Castoldi, M. & Popov, A. V. Purification of brain tubulin through two cycles of polymerization- depolymerization in a high-molarity buffer. *Protein Expr. Purif.* **32**, 83–88 (2003).

100. Gell, C. *et al. Microtubule dynamics reconstituted in vitro and imaged by single-molecule fluorescence microscopy*. *Methods in Cell Biology* vol. 95 (Elsevier, 2010).

101. Hyman, A. A., Salser, S., Drechsel, D. N., Unwin, N. & Mitchison, T. J. Role of GTP hydrolysis in microtubule dynamics: Information from a slowly hydrolyzable analogue, GMPCPP. *Mol. Biol. Cell* **3**, 1155–1167 (1992).

102. Schindelin, J. *et al.* Fiji: An open-source platform for biological-image analysis. *Nat. Methods* **9**, 676–682 (2012).

103. Rueden, C. T. *et al.* ImageJ2: ImageJ for the next generation of scientific image data. *BMC Bioinformatics* **18**, 1–26 (2017).

104. Bartlett, N. W. & Wood, R. J. Comparative analysis of fabrication methods for achieving rounded microchannels in PDMS. *J. Micromechanics Microengineering* **26**, 1–8 (2016).

105. Gittes, F., Mickey, B., Nettleton, J. & Howard, J. Flexural rigidity of microtubules and actin filaments measured from thermal fluctuations in shape. *J. Cell Biol.* **120**, 923–934 (1993).

106. VanBuren, V., Cassimeris, L. & Odde, D. J. Mechanochemical model of microtubule structure and self-assembly kinetics. *Biophys. J.* **89**, 2911–2926 (2005).

107. Dye, R. B., Fink, S. P. & Williams, R. C. Taxol-induced flexibility of microtubules and its reversal by MAP-2 and Tau. *J. Biol. Chem.* **268**, 6847–6850 (1993).

108. Venier, P., Maggs, A. C., Carlier, M. F. & Pantaloni, D. Analysis of microtubule rigidity using hydrodynamic flow and thermal fluctuations. *J. Biol. Chem.* **269**, 13353–13360 (1994).

109. Gall, J. G. Microtubule fine structure. *J. Cell Biol.* **31**, 639–643 (1966).

110. Ledbetter, M. C. & Porter, K. R. A 'microtubule' in plant cell fine structure. *J. Cell Biol.* **19**, 239–250 (1963).

111. Cooper, G. *The Cell: A Molecular Approach*. (Sinauer Associates, Inc., 2000).

112. Mickey, B. & Howard, J. Rigidity of microtubules is increased by stabilizing agents. *J. Cell Biol.* **130**, 909–917 (1995).

113. Kikumoto, M., Kurachi, M., Tosa, V. & Tashiro, H. Flexural rigidity of individual microtubules measured by a buckling force with optical traps. *Biophys. J.* **90**, 1687–1696 (2006).

Appendix A

Photolithography and Microfabrication Protocol

The goal of this appendix is to outline a step-by-step standard operating procedure for the creation of the two-layered microfluidic device outlined in this thesis by: (1) using photolithography techniques to create microfluidic device masters on silicon wafers, and (2) using microfabrication techniques to create functional two-layered devices in PDMS. Note that the work detailed in this protocol was performed in the Vanderbilt Institute of Nanoscale Science and Engineering (VINSE) core Class 100 cleanroom using their equipment and setup at the time. It is feasible that the equipment, location, materials, etc. may change with time, but the general setpoints and directions of this protocol should remain consistent. While a general knowledge of the processes is assumed, each stage gate in the process is outlined in a series of sections below, with each section having a series of numbered steps containing the action to be performed (bolded and fully capitalized) and the setpoint/button to be verified/manipulated (italicized) during that step. The entire protocol is estimated to take 3 days to complete: sections 1-6 on Day 1, sections 7-10 on Day 2, and section 11 on Day 3.

Photolithography

1. Plasma cleaning silicon wafers

Clean silicon wafer(s) in Trion Phantom ICP-RIE using the following steps (silicon wafers are 3" diameter, single side polished (SSP), <1 0 0> orientation). Cleaning the wafers in this way removes any debris or residue from the surface.

NOTE: Always use tweezers when moving the silicon wafer during photolithography processes. To move/pick up the silicon wafer, manipulate with tweezers from the side of the wafer and nudge the wafer until able to get a firm hold on the smallest area of the wafer possible to be moved safely. Also minimize touching the shiny surface of the wafer, to prevent scratching.

1.1. **VERIFY** base pressure is < *5E-05 Torr* and equipment is in *Standby Mode* (located on the display screen).

1.1.1. If base pressure is not low enough, **CONTACT** VINSE staff.

1.2. **SELECT** *Cancel* on the display screen to exit Standby Mode.

1.3. **VERIFY** both switches on the machine front panel (below the screen, the panel door swings down) are set to *Auto*.

1.3.1. If the switches' as-found positions are *Manual*, **SWITCH** them to *Auto* now.

1.4. **SELECT** *Files > O2 clean* on the display screen.

1.5. **VERIFY** that the *O2 clean* recipe name is displayed on the screen.

1.6. **SELECT** *Exit* on the display screen.

1.7. **SELECT** *Vent Reactor* on the display screen.

1.8. **WAIT** until chamber lid opens.

1.9. **PLACE** silicon wafers shiny side up on the carrier wafer.

1.10. **VERIFY** carrier wafer is centered on chuck.

1.11. **SELECT** *Close Lid* on the display screen.

1.12. **WAIT** until lid is completely closed.

1.13. **SELECT** *Automatic Process Control* on the display screen.

1.14. **VERIFY** that the *Ion gauge* reaches a value of < *5E-05 Torr* on the display screen.

1.15. **VERIFY** process gas flow begins and set point pressure is reached on the display screen.

1.16. **VERIFY** RF power turns on, on the display screen.

1.17. **VERIFY** *ICP* and *RIE* reflected power are both *< 5 W* and *DC bias* is *200-250V*, or no more than 10% deviation from these values, on the display screen.

NOTE: If these values deviate by more than 10%, **CONTACT** VINSE staff to let them know of the issue, but continue with subsequent steps.

1.18. **VERIFY** plasma is on, the correct color (a purple-pink glow), and there is no sparking/flickering (you can see this by looking in the side viewing port).

1.19. **WAIT** until process is complete, approximately 5 minutes.

1.20. **SELECT** *OK* on the display screen.

1.21. **SELECT** *Vent Reactor* on the display screen.

1.22. **WAIT** until chamber lid opens.

1.23. **REMOVE** silicon wafers from plasma cleaner.

NOTE: From this point on, keep wafers in Petri dishes with lids covered whenever not in use.

1.24. **SELECT** *Close Lid* on the display screen.

1.25. **WAIT** until lid is completely closed.

1.26. **SELECT** *Standby* on the display screen.

1.27. **VERIFY** tool reaches *Standby Mode* on the display screen.

2. HMDS treatment of silicon wafers

Treat the silicon wafers in the YES HMDS (hexamethyldisilazane) Oven using the following steps. HMDS coating helps facilitate photoresist adhesion to the silicon wafer.

2.1. **VERIFY** HMDS oven is *on* and at *150°C* (located on the front panel).

2.2. If the oven is not on, **TURN ON** HMDS oven:

2.2.1. **RELEASE** *red EMO switch* by twisting to the right.

2.2.2. **PRESS** the *green Power On* button.

2.2.3. **WAIT** until the system controller has booted up and displays *Reset State* on the screen.

2.3. If the oven is not at *150°C*, **SET** the HMDS oven temperature:

2.3.1. **PRESS** and **HOLD** the *star button* on the temperature controller until the set point temperature is displayed.

2.3.2. With the star button held, **PRESS** either the *up or down arrow* until *150* is displayed.

2.4. **VERIFY** HMDS vessel is not empty and is at low pressure (HMDS liquid is located in the clear panel to the left of oven door).

NOTE: If the HMDS vessel is empty, **CONTACT** VINSE staff and wait for instructions.

2.5. **PLACE** silicon wafers into oven in provided metal wafer carriers or directly on oven shelf, with the shiny side of the wafers up.

2.6. **CLOSE** the HMDS oven door.

2.7. **WAIT** 5 minutes for the sample temperature to equilibrate.

2.8. **SELECT** *Enter Recipe Number* radio button on the operator panel.

2.9. **ENTER** recipe number *01*, which corresponds to *HMDS Prime Process*, on the operator panel.

2.10. **SELECT** *Press to Start* button on the operator panel. The green light on the light tree above the HMDS oven will illuminate.

2.11. **WAIT** until the yellow light is illuminated on the light tree, approximately 30 minutes.

2.12. **REMOVE** the sample carrier and/or silicon wafers, using tweezers and/or thermal mittens.

2.13. **CLOSE** HMDS oven door.

2.14. **SELECT** *Press to Reset* radio button on the operator panel, which should turn off the yellow light on the tower.

2.15. **VERIFY** no light is illuminated on tower, the sample carrier is returned to shelf beneath oven (if it was used), and the HMDS oven door is closed.

3. Deposit and spin photoresist

Deposit SPR 220 7.0 photoresist onto silicon wafers using the following steps. SPR is a positive photoresist with relatively low melting point suitable for resist reflow.

3.1. **RETRIEVE** a bottle of SPR 220 7.0 photoresist (under the photolithography hood), and a sheet of aluminum foil, a 1 mL plastic syringe for each silicon wafer that will be used, and a wipe (all on the table across from the photolithography hood).

NOTE: If the photolithography hood is not on, **CONTACT** VINSE staff.

3.2. **OPEN** the spin coater lid in the photolithography hood, if not already open.

3.3. **LINE** the bottom of the spin coater with the aluminum foil, punching a hole in the middle of the foil as necessary to completely cover the bottom and sides of the spin coater.

3.4. **RETRIEVE** 3” black chuck piece (from briefcase on table across from photolithography hood) and place on the spin coater strut**.**

3.5. **PLACE** silicon wafer on the chuck, shiny side up, attempting to center it.

3.6. **SELECT** *Start Centering* on the spin coater operator panel. This will turn on a vacuum to hold the wafer in place and spin the strut for a few seconds.

3.7. **OBSERVE** the spinning wafer as it spins; if the path is very elliptical, it is not aligned well and will result in a non-homogenous distribution of resist across the wafer. Repeat the steps below until the wafer spins a near-circular route:

3.7.1. **SELECT** *Vacuum Off* on the operator panel.

3.7.2. **MOVE** the wafer on the chuck to better center it.

3.7.3. **SELECT** *Start Centering* on the operator panel.

3.7.4. **OBSERVE** the spinning wafer to determine if it is better centered.

3.8. **OPEN** the bottle of SPR 220 7.0.

3.9. **SQUEEZE** the plastic syringe bulb to expel any air.

3.10. **WHILE** still squeezing the syringe bulb, **SUBMERGE** the syringe tip into the SPR 220 7.0.

3.11. **RELEASE** the syringe bulb slowly to draw the photoresist into the syringe.

3.12. **ONCE** the syringe is around three-quarters full, gently REMOVE the syringe from the photoresist, keeping the bulb partially depressed so that no air comes into the syringe.

3.13. **SQUEEZE** the syringe bulb slowly above the silicon wafer to deposit the photoresist on the center of the silicon wafer.

NOTE: Avoid bubbles by keeping the tip of the syringe in contact with the photoresist on the wafer, and do not over-press the syringe bulb after the last of the photoresist is expelled.

3.14. **CLOSE** the spin coater lid.

3.15. **SELECT** *Recipe* on the operator panel.

3.16. **SELECT** *SPR 220_45_1000* for shorter features (approximately 10 μm, used for the channels wafer) or *SPR 220_45_750* for taller features (approximately 14 μm, used for the valves wafer).

3.17. **SELECT** *Run Recipe* on the operator panel.

3.18. **WAIT** until the recipe completes (a persistent beeper will sound on the operator panel).

3.19. **SELECT** *Okay* on the operator panel.

3.20. **MOVE** the wafer from the spin coater to the heating element on the first hot plate to the right of the spin coater.

3.21. **TURN ON** the first hot plate, if it is not on already, and specify a setpoint of *~70 ˚C*.

3.22. **TURN ON** the second hot plate, if it is not on already, and specify a setpoint of *~70 ˚C*.

NOTE: The temperature setpoint can be adjusted by simultaneously pressing the "*" button and the *up/down arrow* buttons on the front face of the hot plate.

3.23. **REPEAT** steps 3.5-3.20 for each silicon wafer, adjusting the spin coater recipe as needed to yield desired feature heights and putting all wafers on the same hot plate.

3.24. Once all wafers have been spin-coated, **INCREASE** the temperature on the first hot plate in *10 ˚C* increments until *115 ˚C*, waiting 3-5 minutes between each increment.

NOTE: When finished using the spin coater, dispose of aluminum foil and photoresist in appropriate container and clean the spin-coater using IPA and a wipe.

3.25. **TURN OFF** the first hot plate.

3.26. **WAIT** until the temperature of the first hot plate is below *80 ˚C* (the current temperature can be seen by cycling the power of the hot plate).

NOTE: From here on, periodically observe the wafers to check for cracking of the photoresist. SPR cracks very easily while cooling, especially at these high photoresist thickness. Cracks will adversely affect the photoresist exposure and development. If cracking occurs, turn on and increase the temperature of the current hot plate by 10 ˚C and wait 5 minutes. Check if the cracks re-melt. If so, continue the subsequent steps. If the cracks persist, increase the temperature of the hot plate by another 10 ˚C and wait 5 more minutes. Repeat this until the cracks re-melt. If cracking during cooldown persists, wait longer time periods between executing subsequent cooling steps.

3.27. **TRANSFER** the wafers to the heating element on the second hot plate, which should still be on and set at *~70 ˚C*.

3.28. **WAIT** 10 minutes.

3.29. **TURN OFF** the second hot plate.

3.30. **WAIT** until the temperature of the second hot plate is below *65 ˚C* (the current temperature can be seen by cycling the power of the hot plate).

3.31. **SET** the Petri dishes on the side of the second hot plate (instead of on the heating element like the wafers are). This will allow the Petri dishes to warm as well and lower the thermal shock to the wafers.

3.32. **TRANSFER** the wafers to the side of the second hot plate (instead of on the heating element).

3.33. **WAIT** until the temperature of the second hot plate is below *50 ˚C* (the current temperature can be seen by cycling the power of the hot plate).

3.34. **TRANSFER** the wafers into the Petri dishes.

3.35. **TRANSFER** the Petri dishes with wafers to a surface that is *not* a stainless-steel table (i.e., on top of a few wipes, on a binder, on the keyboard of a laptop, etc.). This will help prevent heat shock as well.

4. UV exposure of photoresist

Expose the photoresist-deposited wafers using the following steps:

4.1. **TURN ON** mask aligner main power supply (the switch is labeled on the mask aligner), if it is not already on.

4.2. **TURN ON** mask aligner lamp power supply (underneath the mask aligner), if it is not already on.

4.3. If the mask aligner was not already on, **SWITCH** green electronic power switch to *On* (it is a spring switch, so it will release back).

4.4. **WAIT** until the mask aligner screen displays *"Ready for start – press load button"*.

4.5. **PRESS** the *Load* button on the mask aligner control panel.

4.6. **WAIT** until *"Ready for load"* is displayed on the mask aligner screen.

4.7. **PULL** the wafer chuck drawer of the mask aligner stack outwards until it clicks (the drawer can be identified by it having a handle to help pull it out).

4.8. **LOAD** the 3" wafer chuck piece onto the wafer chuck drawer, if not already loaded (the piece should be located on the table next to the mask aligner).

4.9. **VERIFY** the wafer chuck piece is centered (the cutout in the chuck perimeter should be in the front middle of the stage; there is an indicator pin on the stage to help with this).

4.10. **PUSH** the wafer chuck drawer back into the mask aligner.

4.11. **VERIFY** the stage x- and y-knobs are at *"10"* position (located on the lower left and right of the mask aligner stage platform).

4.12. **VERIFY** the stage θ-knob is *centered* (located on the lower front of the mask aligner stage platform).

4.13. **RETRIEVE** optical power meter from the table next to the mask aligner.

4.14. **TURN ON** the optical power meter.

4.15. **PLACE** the power meter face-up in the center of the chuck piece on the mask aligner control panel.

4.16. **PRESS** the *Lamp Test* button on the mask aligner control panel. This will move the light source forward over the stage and turn on the UV lamp.

NOTE: Avoid looking directly at UV lamp to prevent eye strain.

4.17. **RECORD** the optical power reading from the meter in the notebook on the table next to the mask aligner.

4.18. **PRESS** the *Lamp Test* button on the mask aligner control panel. This will turn off the UV lamp and move the light source back.

4.19. **TURN OFF** and **REPLACE** optical power meter.

4.20. **UNLOAD** the mask holder, if it is not already, by **PULLING** it out from its grooved drawer on the mask aligner control panel just above the stage with the chuck piece.

4.21. If the mask holder was not already unloaded, **INVERT** the mask holder and **PLACE** onto the stand on the left side of the mask aligner.

4.22. **PRESS** the *Change Mask* button on the mask aligner control panel.

4.23. **WAIT** until *"Press enter to toggle mask vacuum"* is displayed on the mask aligner control panel screen.

4.24. **PRESS** the *Enter* button on the mask aligner control panel to turn the mask vacuum off.

NOTE: This mask vacuum is intended to hold the mask in place during operations; the vacuum needs to be off for putting the mask onto the holder, but the vacuum must be on before moving the holder with mask back into the mask aligner.

4.25. **LOAD** mask onto mask holder, **ENSURING** that the feature side is facing upwards.

4.26. **PRESS** the *Enter* button on the mask aligner control panel to turn the mask vacuum on.

4.27. Carefully **LOAD** the mask holder back into its grooved drawer on the mask aligner control panel stage.

4.28. **PRESS** the *Change Mask* button on the mask aligner control panel.

4.29. **VERIFY** mask holder is in place by gently pulling on it; the mask holder should not move. If it does move, **CONTACT** VINSE staff.

4.30. **PRESS** the *Load* button on the mask aligner control panel.

4.31. **WAIT** until *"Pull slide and load substrate onto chuck"* is displayed on the mask aligner control panel screen.

4.32. **PULL** out the drawer with the wafer chuck piece.

4.33. **LOAD** the appropriate wafer for the corresponding mask onto the wafer chuck using the alignment pins on the chuck to ensure the wafer is flat and aligned appropriately.

4.34. **PRESS** the *Enter* button on the mask aligner control panel to turn on a vacuum to keep the wafer in place on the chuck.

4.35. **PUSH** the wafer chuck drawer back into the mask aligner.

4.36. **PRESS** the *Enter* button on the mask aligner control panel.

4.37. **WAIT** while mask aligner lifts the wafer into position below the mask. During this time, the mask aligner screen will display *"Performing WEC please wait"*.

4.38. **VERIFY** *"Align substrate"* is displayed on the mask aligner screen and the yellow light next to the display is *lit* to signify contact.

4.39. **PRESS** the *Select Program* button on the mask aligner control panel.

4.40. **SET** the *"Expose Type"* parameter on the mask aligner screen to *"Hard-Ct/Cont"* by **PRESSING** the *up/down arrow buttons* on the mask aligner control panel.

4.41. **PRESS** the *Select Program* button on the mask aligner control panel.

4.42. **PRESS** the *Edit Parameter* button on the mask aligner control panel.

4.43 **SET** the *"Exp. Time [s]"* parameter by using the following formula and **PRESSING** the *up/down arrow buttons* on the mask aligner control panel until the correct time is displayed: $Exposure\ time\ (s) = \frac{Desired\ Energy\ (\frac{mJ}{cm^2})}{Lamp\ Power\ (\frac{mW}{cm^2})}$. The desired energy for the valves master, since it should be thicker, is approximately *450 mJ/cm^2*, while the desired energy for the shorter, channels master is approximately *400 mJ/cm^2*. The lamp power is the value recorded using the optical power meter from step 4.17. Round exposure time up to the nearest tenth of a second.

4.44. Once the appropriate exposure time is displayed, **PRESS** the *Edit Parameter* button on the mask aligner control panel.

4.45. **VERIFY** that the yellow light to the left of the display is still *lit* and that *"Hard-Ct/Cont"* and the *desired exposure time* are displayed on the mask aligner screen.

4.46. **PRESS** the *Expose* button on the mask aligner control panel. This will move the light source forward over the stage and turn on the UV lamp.

NOTE: Avoid looking directly at UV lamp to prevent eye strain.

4.47. **WAIT** until the exposure is complete and the light source automatically moves back to its original position. *"Pull slide and unload exposed substrate"* should be displayed on the mask aligner screen.

4.48. **PULL** out the wafer chuck drawer.

4.49. **REMOVE** the exposed wafer from chuck and **PLACE** the wafer in a Petri dish.

4.50. **PUSH** the wafer chuck drawer back into the mask aligner.

4.51. **PRESS** the *Change Mask* button on the mask aligner control panel.

4.52. **VERIFY** *"Press enter to toggle mask vacuum: on"* is displayed on the mask aligner screen.

4.53. Carefully **PULL** the mask holder out from its grooved drawer on the mask aligner control panel, just above the stage with the chuck piece.

NOTE: While the mask should still be connected to the holder via the vacuum, place a hand underneath the mask to prevent damage if the vacuum fails.

4.54. **INVERT** the mask holder and **PLACE** onto the stand on the left side of the mask aligner.

4.55. **PRESS** the *Enter* button on the mask aligner control panel to turn the mask vacuum off.

4.56. **REMOVE** the mask from the mask holder.

4.57. **REPEAT** steps 4.25 – 4.56 for all wafers that will be exposed, ensuring the correct mask is used for the correct wafer.

4.58. Once all exposures are complete and the final mask has been removed from the mask holder, **PRESS** the *Change Mask* button on the mask aligner control panel.

4.59. **VERIFY** *"Mask holder not inserted or not in correct position! Confirm with enter"* is displayed on mask aligner screen.

4.60. **PRESS** the *Enter* button on the mask aligner control panel. The mask aligner can now be left in this state.

5. Photoresist rehydration

After exposure, allow the photoresist to rehydrate using the following steps.

5.1. **SET** the exposed silicon wafers in their Petri dishes beneath an inverted Tupperware container with one side cut out.

5.2. **PARTIALLY OPEN** the Petri dishes about ¾ of the way by resting one end of the lid on the ground with the other end propped up on the base of the Petri dish.

5.3. **WAIT** 4 hours for rehydration to occur.

NOTE: If you leave during the rehydration time, write a note for others asking them not to move the wafers and include your name, date, phone number, and time you will return. Set the note near the wafers.

6. Post-exposure photoresist bake

After the 4-hour rehydration, post-exposure bake the exposed wafers using the following steps.

6.1. **TURN ON** a hotplate in the photolithography hood, if one is not on already, and specify a setpoint of *~50 ˚C*.

6.2. **SET** the wafers onto the heating element on the hot plate.

6.3. **INCREASE** the temperature on the first hot plate in *10 ˚C* increments until *115 ˚C*, waiting ~3 minutes between each increment.

6.4. **WAIT** for the wafers to incubate at *115 ˚C* for 10 minutes.

6.5. **CREATE** a 'cover' by molding a sheet of aluminum foil around a 100x50 Pyrex dish (create as many covers as you have wafers).

6.6. **TURN OFF** the hot plate.

6.7. **COVER** the wafers with the aluminum foil 'cover'.

6.8. **ALLOW** the wafers to cool ambiently overnight. This will allow the wafers to slowly cool without thermally cracking the photoresist.

NOTE: This completes the steps required for the first day of fabrication. It is recommended to proceed to Development the following day. If you leave, write a note for others asking them not to move the wafers and include your name, date, phone number, and time you will return. Set the note near the wafers.

7. Photoresist development

Develop the photoresist on the wafers using the following steps.

7.1. **RETRIEVE** a clean plastic container and a lid (from the Development hood, the lid should be labeled *'MF-319'*). If there is not a container labeled *'MF-319'*, **CREATE** and **LABEL** a new container using materials from the VINSE storage cabinet.

NOTE: If the development hood is not on, **CONTACT** VINSE staff.

NOTE: If more than one wafer is being developed, multiple plastic containers can be used at once, provided they were initially clean and have lids. Alternatively, the same container can be used for multiple wafers in sequence, but the MF-319 developer must be replaced between each wafer. It is not recommended to develop multiple wafers in the same container simultaneously, as scratching of the photoresist can occur.

7.2. **RETRIEVE** MF-319 developer (from underneath the Development hood).

7.3. Carefully **POUR** the MF-319 developer into the plastic container until the container is approximately halfway full.

7.4. **PUT AWAY** the MF-319 developer (underneath the Development hood).

7.5. **CLOSE** the plastic container using the lid.

7.6. Gently **SWIRL** the plastic container for 30 minutes, keeping the bottom of the container on the surface of the development hood and sliding it around gently.

NOTE: Switch the direction of shaking periodically, to ensure complete development. Alternatively, a standing mixer can be programmed to agitate the container for the time period, if one is available in the development hood.

7.7. **DISPOSE** of MF-319 developer in the appropriate drain (the drain is at the right side of the Development hood and should be labeled as *'Developer'*).

7.8. **REPEAT** steps 7.2 – 7.7 until no more photoresist is removed from the wafers (indicated by the MF-319 solution not becoming any more colored over time, and the wafers being visibly stripped of photoresist except for the device design).

7.9. **REMOVE** the wafers from the plastic containers.

7.10. **RINSE** the wafers with DI water (from the DI gun at the right side of the development hood) for 30 seconds.

7.11. **DRY** the wafers with Nitrogen gas (from the N_2 gun at the right side of the development hood).

7.12. Once all wafers have been developed, **DISPOSE** of any leftover MF-319 developer in the appropriate drain (the drain is at the right side of the development hood and should be labeled as *'Developer'*).

7.13. **CLEAN** the plastic containers and lids using DI water (from the DI gun at the right side of the development hood) 3 times and hang up on pegs or set on wipes to dry.

8. Positive resist reflow

Perform a positive resist reflow technique using the following steps. Resist reflow helps create more rounded features in the photoresist.

8.1. **TURN ON** both hotplates in the photolithography hood, if they are not on already, and specify a setpoint of *~70 ˚C* on both hotplates.

NOTE: If the photolithography hood is not on, **CONTACT** VINSE staff.

NOTE: The temperature setpoint can be adjusted by simultaneously pressing the * button and the *up/down arrow* buttons on the front face of the hot plate.

8.2. **SET** the masters onto the heating element of one hot plate.

8.3. **INCREASE** the temperature on this hot plate in *10 ˚C* increments until *115 ˚C*, waiting ~3 minutes between each increment.

8.4. **WAIT** for the masters to incubate at *115 ˚C* for 15 minutes.

8.5. **TURN OFF** the first hot plate.

8.6. **WAIT** until the temperature of the first hot plate is below *80 ˚C* (the current temperature can be seen by cycling the power of the hot plate).

8.7. **TRANSFER** the masters to the heating element on the second hot plate, which should still be on and set at *~70 ˚C*.

8.8. **WAIT** 10 minutes.

8.9. **TURN OFF** the second hot plate.

8.10. **WAIT** until the temperature of the second hot plate is below *65 ˚C* (the current temperature can be seen by cycling the power of the hot plate).

8.11. **TRANSFER** the masters to the side of the second hot plate (instead of on the heating element).

8.12. **WAIT** until the temperature of the second hot plate is below *50 ˚C* (the current temperature can be seen by cycling the power of the hot plate).

8.13. **TRANSFER** the masters into the Petri dishes.

9. Silanize masters

Silanize the masters using the following steps. Silanization facilitates easy liftoff of PDMS from the masters, especially when the PDMS is very thin.

9.1. **SET UP** the desiccator in the microfluidics hood. Make sure to **CONNECT** the vacuum line to the microfluidics hood's vacuum port.

NOTE: If the photolithography hood is not on, **CONTACT** VINSE staff.

9.2. **RETRIEVE** the bottle of trichloro(1H, 1H, 2H, 2H-perfluorooctyl) silane from the chemical storage cabinet, an aluminum dish, a wipe, and a pipet.

9.3. **REMOVE** the masters from their Petri dishes and **SET** them in the desiccator in the microfluidics hood.

9.4. **SET** the aluminum tin in the desiccator.

9.5. **PIPET** one drop of the silane solution into the aluminum tin.

9.6. **CLOSE** the desiccator and **START** vacuum.

NOTE: Dispose of the pipet of in appropriate container and return the silane solution to the chemical storage cabinet.

9.7. **WAIT** for 2 hours for silanization to complete.

NOTE: If you leave during the silanization time, write a note for others asking them not to move the system and include your name, date, phone number, and time you will return. Set the note near the desiccator.

9.8. After 2 hours of silanization, **TURN OFF** the microfluidics hood vacuum.

9.9. Slowly **OPEN** the bleed valve on the desiccator to gently break vacuum.

9.10. **PLACE** masters back into Petri dishes and **DISPOSE** of the aluminum tin in appropriate container.

NOTE: Silanization may need to be repeated periodically on the masters, and more frequently on devices where thinner layers of PDMS are used. If stickiness of PDMS is noticed when removing the PDMS from the masters, the masters may need re-silanized and this section should be re-performed once all PDMS has been removed from the wafers.

NOTE: This completes the steps required for photolithography. The master wafers can be used repeatedly to make PDMS devices until degradation requires creation of new masters.

Microfabrication

10. Depositing PDMS

Deposit PDMS onto the device masters using the following steps.

NOTE: If there is residual PDMS on the masters from a previous microfabrication, the residual PDMS must first be removed and disposed of prior to pouring new PDMS onto the masters.

10.1. In the miscellaneous flow hood (near the back of VINSE), **WEIGH** approximately *20 g* of PDMS elastomer into a plastic cup using the scale.

NOTE: The scale may not be set up in the hood; if it is not, **SET UP** and **PLUG IN** the scale in the hood.

NOTE: **ZERO** the scale before weighing any materials and in between any materials.

10.2. In the same plastic cup, **WEIGH** *10%* of the PDMS elastomer weight of PDMS curing agent solution (this value should be around *2 g*, giving a PDMS:curing agent ratio of *10:1*).

10.3. **HAND MIX** the two solutions together in the plastic cup using a plastic stirrer for 5 minutes.

10.4. After 5 minutes of mixing, **SET UP** desiccator in fume hood. Make sure to **CONNECT** the desiccator vacuum line to the fume hood's vacuum port and **TURN ON** the vacuum valve.

10.5. **PLACE** the plastic cup of PDMS solution into the desiccator.

10.6. **TURN ON** fume hood vacuum.

10.7. **ENSURE** that the desiccator is well sealed and that a vacuum is present.

NOTE: If vacuum is not present, **CONTACT** VINSE staff for help.

10.8. **WAIT** 30 minutes for desiccation to complete.

10.9. After 30 minutes of desiccation, **TURN OFF** the fume hood vacuum.

10.10. Slowly **OPEN** the bleed valve on the desiccator to gently break vacuum (at this point, there should be few if any bubbles still visible in the PDMS solution).

10.11. **REMOVE** the plastic cup from the desiccator.

10.12. **PUT AWAY** the desiccator.

10.13. If the master needs to be spin-coated with PDMS (the primary channel master), **PROCEED** with the steps below. If the PDMS does not need spin coated on the wafer (the Quake valves master), **SKIP** to step 10.14.

NOTE: Usually, for making PDMS for both the channels and the valves masters, a small dollop (i.e. only a couple grams) of PDMS will be used for the channels masters, while the remaining bulk of the PDMS will be poured onto the valves master.

10.13.1. **SET UP** the PDMS spin coater in the fume hood. Make sure to **PLUG IN** the spin coater power, **CONNECT** the vacuum line to the fume hood's vacuum port, **TURN ON** the vacuum valve, **CONNECT** the air line to the fume hood's air port, and **TURN ON** the air valve.

10.13.2. **PLACE** the master wafer onto the spin coater loading column.

10.13.3. **PRESS** the *Vacuum* button on the spin coater to turn on the vacuum and hold the master in place.

10.13.4. Manually **SPIN** the spin coater loading column to **ENSURE** the master is well-centered on the loading column.

NOTE: The master may need slight adjustments to center it on the loading column. If this is necessary, **PRESS** the *Vacuum* button on the spin coater to turn off the vacuum prior to adjusting; **PRESS** the *Vacuum* button on the spin coater again to turn vacuum back on prior to proceeding to next steps.

10.13.5. Once the master is well-centered, **POUR** a small dollop (less than 25% of the total volume) of PDMS solution onto the center of the master.

10.13.6. **PRESS** the *Program Select* button on the spin coater until a recipe is displayed with only *1* step, a *2000 RPM* spin speed, a *30-second* spin time, and an acceleration of *1040*.

10.13.7. **CLOSE** the spin coater lid.

10.13.8. **PRESS** the *Run/Stop* button on the spin coater.

10.13.8. **WAIT** until the recipe completes.

10.13.9. **OPEN** the spin coater lid and **PRESS** the *Vacuum* button to turn off the vacuum.

10.13.9. **PLACE** the PDMS-coated master back in its Petri dish.

10.13.10. **PUT AWAY** the spin coater.

10.14. **POUR** the remaining mixed PDMS from the cup into the Petri dish with the valves master.

10.15. **DISPOSE** of all PDMS and associated components (including gloves) in the appropriate containers.

10.16. **INCUBATE** the masters at *65 ˚C* overnight to allow PDMS to fully cure.

11. Assembling devices

Assemble the PDMS microfluidic devices using the following steps.

11.1. **RETRIEVE** the device masters that have cured PDMS on them, a pair of forceps, and a scalpel/razor blade.

11.2. Carefully **CUT** out the Quake valve PDMS from its mold. Each piece of PDMS should have a little room on each side flanking the device features to facilitate good bonding contact, but the piece also needs to fit on a 22x22 mm glass coverslip.

NOTE: It is undesirable to touch the bottom surface of the PDMS (the surface where the features are), so handle the PDMS with tweezers. Also, never place the PDMS feature-side down against a surface, but whenever the PDMS piece is not in use, turn the PDMS feature side up until it's ready to be used.

11.3. **PUNCH** inlet/outlet holes in the PDMS using a clean 1.5 mm hole punch.

NOTE: Dispose of PDMS pieces in the appropriate waste bin. Also make sure to punch through the device PDMS into a spare layer of sacrificial PDMS rather than into a hard surface that could damage the hole punch.

11.4. If this is the first use of a new channels master wafer, **RETRIEVE** a diamond-tipped blade to carefully break the wafer in half using the following steps. If the wafer is already in two pieces, **SKIP** to step 11.5.

NOTE: The channels master wafer must be broken in half because it cannot fit into the plasma cleaner as a single piece.

NOTE: If a diamond-tipped blade cannot be found, **CONTACT** VINSE staff for assistance.

11.4.1. Carefully **DRAW** a line through the thin layer of PDMS down the middle of the channel masters wafer using the diamond-tipped blade. This should result in a visible scratch on the wafer and cut through the PDMS along the line.

11.4.2. **RE-TRACE** a couple more scratches on the same line at the two ends of the wafer. This will make the wafer easier to break along the line.

11.4.3. Carefully **SET** the channels wafer on a slightly raised surface, such as a Petri dish lid, with the wafer laying halfway off the lid. The setup should result in half of the wafer resting on the raised surface and the other half extended over the edge, with the scratched line just at the edge.

11.4.4. Lightly **TAP** the portion of the wafer that is extended over the ledge until the wafer splits in two. This should result in a clean break between the two halves of the wafer. If the wafer shatters, that's rough buddy. Will have to start the photolithography process again with a new wafer and/or use the undamaged portion of the wafer.

11.5. After all the valve devices have been punched, **TRANSFER** the punched valve devices, channels master halves, and forceps to the custom PDMS aligner in the microfabrication suite.

11.6. Also **RETRIEVE** a Sharpie marker.

11.7. **CLEAN** the blank glass plate labeled *'PDMS aligner'* with IPA and a wipe.

NOTE: If the PDMS aligner glass plate cannot be found, **CONTACT** VINSE staff for assistance.

11.8. **LOG** into the PDMS aligner laptop.

NOTE: If you are unable to login to the laptop, **CONTACT** VINSE staff for assistance.

11.9. **LAUNCH** the DinoCapture software on the laptop.

11.10. **PLACE** one half of the channels master on the custom PDMS aligner microscope.

11.11. **CENTER** the channels master in the field of view of the microscope, adjusting the focus, light intensity, and/or the stage position, as necessary.

11.12. **PLACE** a single punched valves piece of PDMS onto the glass plate, with the feature side of the PDMS facing up.

NOTE: Make sure the PDMS adheres to the surface of the glass plate, as the next step will be to invert the glass plate.

11.13. Carefully **INVERT** the glass plate and **PLACE** onto the adjustable frame of the custom PDMS aligner (the frame can be raised/lowered using the adjacent knobs).

NOTE: Take care to not touch the surface of the valves PDMS to the surface of the channels master wafer; have the adjustable frame raised high enough to prevent the PDMS pieces from touching.

11.14. Slowly **LOWER** the adjustable frame with the valves PDMS piece until it is just above, but not touching, the channels master. **OBSERVE** the alignment of the two layers using the software (shown by the alignment markings included in both layers of PDMS) and **ADJUST** the stage x-, y-, and θ-axes, as necessary.

NOTE: There is a counterweight lever near the adjustable frame knob that should prevent the frame from free-falling under the weight of the glass plate. Make sure that the knob is in position to prevent the frame from free-falling and adjust as necessary so that the glass plate doesn't descend onto the channels master.

11.15. If the two layers cannot be precisely aligned, **RAISE** the adjustable frame and **MOVE** the PDMS piece and/or the channels master as necessary.

11.16. **REPEAT** steps 11.14 - 11.15 until the two layers are aligned.

11.17. **RAISE** the adjustable frame and **REMOVE** the glass plate from the frame.

11.18. **RE-INVERT** the glass plate so that the feature-side of the valves piece of PDMS is face-up.

11.19. Using the Sharpie marker, **DRAW** onto the surface of the glass plate a faint outline of the valves PDMS piece.

11.20. Using the Sharpie marker, **DRAW** onto the surface of the aligner stage a faint outline of the channels master.

11.21. **VERIFY** the PDMS plasma cleaner is ON. If the plasma cleaner is not on, **TURN ON** the power switches for the main plasma cleaner, then the vacuum pump, then the PlasmaFlo regulator.

11.22. Carefully **PLACE** both the channels master and the punched piece of valves PDMS onto the plasma cleaner carrier wafer, with both the channels master and the valves PDMS piece slightly hanging off the edge of the wafer.

11.23. **PLACE** the carrier wafer into the plasma cleaner.

11.24. **CLOSE** the plasma cleaner door and **ROTATE** the ball valve on the door to point toward the vacuum supply (away from the open inlet).

11.25. **PRESS** the *Run* button on the vacuum control panel

11.26. **WAIT** until the pressure on the plasma cleaner display is < *0.5 Torr*.

11.27. **TURN** the CDA knob on the PlasmaFlo regulator until the flowmeter reads *~20*.

NOTE: Our anecdotal experience favors CDA for all plasma bonding.

11.28. **TURN** the *RF switch* on the plasma cleaner to *High*.

11.29. **WAIT** 40 seconds.

11.30. **TURN** the *RF switch* on the plasma cleaner to *Off*.

11.31. **TURN** the *CDA knob* on the PlasmaFlo regulator until the flowmeter reads *0*.

11.32. **PRESS** the *Run* button on the vacuum control panel.

11.33. **WAIT** until the pressure on the plasma cleaner display only changes by a few Torr (not more than *10 Torr* at a time).

11.34. Slowly **ROTATE** the ball valve from the vacuum line to the open inlet, watching the pressure on the plasma cleaner display and adjusting the ball valve position so that the pressure only increases ~50 Torr at a time until the pressure stops increasing and the chamber door opens.

11.35. Carefully **REMOVE** the plasma cleaner carrier wafer.

NOTE: From this point, the surfaces of the PDMS will remain active for approximately 1 minute. Work deliberately to execute the following steps as rapidly as safely possible.

11.36. **PLACE** the channels master back onto the aligner stage within the outline drawn previously.

11.37. **PLACE** the valves PDMS piece with the feature side facing up back onto the glass plate within the outline drawn previously.

11.38. Carefully **INVERT** the glass plate and **PLACE** onto the adjustable frame of the custom PDMS aligner (the frame can be raised/lowered using the adjacent knobs).

NOTE: Take care to not touch the surface of the valves PDMS to the surface of the channels master wafer; have the adjustable frame raised high enough to prevent the PDMS pieces from touching.

11.39. Slowly **LOWER** the adjustable frame with the valves PDMS piece until it is just above, but not touching, the channels master wafer. **OBSERVE** the alignment of the two layers using the software (shown by the alignment markings included in both layers of PDMS) and **ADJUST** the stage x-, y-, and θ-axes, as necessary.

11.40. Fully **LOWER** the adjustable frame to bring the valves PDMS piece into contact with the channels master and **PRESS** on the glass plate lightly.

11.41. Carefully **REMOVE** the glass plate, valves PDMS piece, and channels master wafer from the aligner stage. The three should be adhered to each other. If something drops off, repeat steps 11.22 - 11.41.

11.42. **INVERT** the glass plate and **PLACE** it on the workbench so that now the channels master is on top with its features facing downward.

11.43, Lightly **TAP** the backside of the channels master to facilitate bonding.

11.44. Using a pair of forceps, carefully **PEEL** the valves PDMS piece away from the glass plate. The channels master should peel away with the valves PDMS piece.

11.45. **INVERT** the valves PDMS piece and channels master and **PLACE** on the workbench so that the channels master is on bottom with its features facing upward.

11.46. Lightly **TAP** the top of the valves PDMS piece to facilitate bonding. Good bonding can sometimes be seen as different areas of the valves PDMS come into contact with the channels PDMS and push air out of the way.

11.47. **INCUBATE** the channels master wafer bound to the valves PDMS piece for 10 minutes at *65 ˚C*.

11.48. After 10 minutes, **REMOVE** the channels master bound to the valves PDMS piece from the incubator.

11.49. Using a scalpel/razor blade, carefully **CUT** the PDMS of the channels master, leaving a few centimeters of space between the valves PDMS piece and the area that is being cut out. Having this extra area will help with lifting off the thin layer of channels PDMS.

11.50. Using tweezers, slowly and carefully **PEEL** the channels PDMS layer away from the master, using the thicker valves PDMS piece as a stable backing to aid in lifting and to prevent tearing the channels PDMS layer.

11.51. Carefully **PUNCH** inlet/outlet holes in the thin channels PDMS layer (punching all the way through the connected valves piece of PDMS) using a clean 1.5 mm hole punch.

NOTE: Use a pair of forceps to hold down the PDMS as you carefully retract the hole punch between punches so that the channels PDMS layer isn't ripped from the valves PDMS piece.

NOTE: Dispose of PDMS pieces in the appropriate waste bin. Also make sure to punch through the device PDMS into a spare layer of sacrificial PDMS rather than into a hard surface that could damage the hole punch.

11.52. After all the inlets/outlets of the channels PDMS have been punched, **TRANSFER** the device and forceps to the custom PDMS aligner in the microfabrication suite.

11.53. **RETRIEVE** a 22x22 mm glass coverslip.

11.54. Carefully **CLEAN** the glass coverslip with IPA wipe.

11.55. **PLACE** the glass coverslip onto the plasma cleaner carrier wafer, with one edge of the coverslip slightly hanging off the edge of the wafer.

11.56. **PLACE** the carrier wafer into the plasma cleaner.

11.57. **CLOSE** the plasma cleaner door and **ROTATE** the ball valve on the door to point toward the vacuum supply (away from the open inlet).

11.58. **PRESS** the *Run* button on the vacuum control panel

11.59. **WAIT** until the pressure on the plasma cleaner display is < *0.5 Torr*.

11.60. **TURN** the CDA knob on the PlasmaFlo regulator until the flowmeter reads *~20*.

11.61. **TURN** the *RF switch* on the plasma cleaner to *High*.

11.62. **WAIT** 5 minutes.

11.63. **TURN** the *RF switch* on the plasma cleaner to *Off*.

11.64. **TURN** the *CDA knob* on the PlasmaFlo regulator until the flowmeter reads *0*.

11.65. **PRESS** the *Run* button on the vacuum control panel.

11.66. **WAIT** until the pressure on the plasma cleaner display only changes by a few Torr (not more than *10 Torr* at a time).

11.67. Slowly **ROTATE** the ball valve from the vacuum line to the open inlet, watching the pressure on the plasma cleaner display and adjusting the ball valve position so that the pressure only increases ~50 Torr at a time until the pressure stops increasing and the chamber door opens.

11.66. Carefully **REMOVE** the plasma cleaner carrier wafer.

11.67. **PLACE** the glass coverslip in a clean Petri dish until ready for use.

11.68. Gently **WIPE** a cleaned glass coverslip and the channels PDMS layer with an IPA wipe.

11.69. Carefully **PLACE** both the PDMS piece and the glass coverslip onto the plasma cleaner carrier wafer, with both the coverslip and the PDMS slightly hanging off the edge of the wafer.

11.70. **PLACE** the carrier wafer into the plasma cleaner.

11.71. **CLOSE** the plasma cleaner door and **ROTATE** the ball valve on the door to point toward the vacuum supply (away from the open inlet).

11.72. **PRESS** the *Run* button on the vacuum control panel

11.73. **WAIT** until the pressure on the plasma cleaner display is *< 0.5 Torr*.

11.74. **TURN** the CDA knob on the PlasmaFlo regulator until the flowmeter reads *~20*.

11.75. **TURN** the *RF switch* on the plasma cleaner to *High*.

11.76. **WAIT** 40 seconds.

11.77. **TURN** the *RF switch* on the plasma cleaner to *Off*.

11.78. **TURN** the *CDA knob* on the PlasmaFlo regulator until the flowmeter reads *0*.

11.79. **PRESS** the *Run* button on the vacuum control panel.

11.80. **WAIT** until the pressure on the plasma cleaner display only changes by a few Torr (not more than *10 Torr* at a time).

11.81. Slowly **ROTATE** the ball valve from the vacuum line to the open inlet, watching the pressure on the plasma cleaner display and adjusting the ball valve position so that the pressure only increases ~50 Torr at a time until the pressure stops increasing and the chamber door opens.

11.82. Carefully **REMOVE** the plasma cleaner carrier wafer.

11.83. Carefully **REMOVE** the plasma cleaner carrier wafer.

NOTE: From this point, the surfaces of the PDMS and glass coverslip will remain active for approximately 1 minute. Work deliberately to execute the following steps as rapidly as safely possible.

11.84. Carefully **INVERT** the PDMS piece and **PLACE** into contact with the glass coverslip, as near the middle of the coverslip as possible.

11.85. Lightly **TAP** the top of the PDMS piece to facilitate bonding. Good bonding can sometimes be seen as different areas of the channels PDMS come into contact with the glass coverslip and push air out of the way.

11.86. **INCUBATE** the completed device at *65 ˚C* overnight.

11.87. **REPEAT** steps 11.10 – 11.86 for each double-layered device to be created.

NOTE: This completes the steps required for microfabrication. The devices have no set shelf life, but it is recommended to store them in a cool, dry area when not in use.

Appendix B

OB1 Flow Controller System Protocols

The goal of this appendix is to outline step-by-step standard operating procedures for the use of our current two channel OB1 flow control system by: (1) calibrating the flowmeters to ensure system fidelity, (2) creating in-house reagent source vials and leak testing, and (3) preparing the system for automated flow control of multiple reagents by using the MUX distribution valve. While a general knowledge of the processes is assumed, each stage gate in the process is outlined in a series of sections below, with each section having a series of numbered steps containing the action to be performed (bolded and fully capitalized) and the setpoint/button to be verified/manipulated (italicized) during that step. Each section of the protocol is estimated to take a few hours.

1. Calibrate flowmeters

Perform a manual calibration of the desired flowmeter(s) using the following steps.

1.1. **OPEN** the compressed air supply tank valve and **ROTATE** the downstream regulator to an outlet value of *50 psig*.

1.2. **TURN ON** the OB1 main power (the power button is on the OB1 box).

1.3. **LAUNCH** the Elveflow software on the computer.

1.4. **CONNECT** the power/data signal cable from the OB1 box to the flow controller.

NOTE: It doesn't matter which channel is being used for the calibration, but it is recommended to switch channels between subsequent calibrations just to make sure both channels are functioning appropriately.

1.5. **VERIFY** the desired channel's air hose is connected from the OB1 box to a port of the reservoir holder, or **CONNECT** this, if needed.

1.6. **FILL** a 1.5 mL Eppendorf vial (the kind with a screw cap) with 1 mL of MilliQ water.

1.7. **ATTACH** the Eppendorf vial to the reservoir holder.

NOTE: This needs to be an airtight seal, so ensure there is an O-ring in the reservoir holder screw fitting and that the tube is tightly secured into the holder.

1.8. **VERIFY** a length of 1/16" outer diameter PEEK capillary resistance tubing is connected through the reservoir holder and into the Eppendorf vial using a ¼-28 fitting and ferrule, or **CONNECT** this, if needed.

1.9. **CONNECT** the PEEK resistance tubing to the desired flowmeter using ¼-28 fitting and ferrule.

1.10. **CONNECT** a length of 1/16" outer diameter Tygon® tubing to the flowmeter using a ¼-28 fitting and ferrule. **PLACE** the other end of this tubing in a waste Eppendorf tube.

1.11. **PRESS** the *Play* button on the Elveflow software to start the OB1 system.

1.12. **ENSURE** the flowmeter is connected to the desired channel on the Elveflow GUI.

1.13. **SET** the desired channel to *flow control*.

1.14. **SET** the desired flow value to *50* (units are in µL/min) and **START** the flow in order to prime the line.

1.15. **WAIT** until flow is seen coming from the outlet of the Tygon® tubing into the waste vial.

1.16. **STOP** the flow.

1.17. **EMPTY** the waste vial.

1.18. **PERFORM** a calibration of the flowmeter by iteratively increasing flowrate values within its operating range using the following steps:

1.18.1. **SET** the desired flow value (units are in μL/min) and START the flow.

1.18.2. **WAIT** 1 minute, and in the meantime **RECORD** the pressure (units are in mbar) required to achieve this flowrate.

NOTE: The pressure will likely fluctuate over time; estimate the pressure to the nearest mbar.

1.18.3. **STOP** the flow.

1.18.4. Manually **MEASURE** the amount of fluid transferred to the waste vial using a pipet. The volume of fluid should be equal to the flow value in μL since flow was run for 1 minute. **RECORD** this volume of fluid, rounding to the nearest μL.

1.18.5. **EMPTY** the waste vial.

1.18.6. **REPEAT** steps 1.18.1 – 1.18.5 twice more for each flowrate, for repeatability.

1.18.7. **REPEAT** steps 1.18.1 – 1.18.6. for each desired flowrate within the flowmeter operation range.

1.19. Manually **GRAPH** the flowrate setpoint versus the pressure required to achieve that flowrate, as well as the flowrate setpoint versus the manually verified volume of solution transferred.

NOTE: Both graphs should be a linear trend, and these values can be used to ensure the flowmeters are functioning appropriately. Furthermore, these graphs can be used to estimate the expected

flowrate value even if a pressure-based control is used in the OB1 system. Since the OB1 system is programmed to maintain a constant upstream pressure, this should result in a constant flowrate even though the volume in the source vial decreases over time.

2. Create reagent source vials for the distribution valve and leak test the system

Create in-house reagent source vials and connect to the MUX distribution valve using the following steps.

2.1. **RETRIEVE** a standard 1.5 mm biopsy punch, some 1.5 mL Eppendorf tubes (the kind with a snap lid), and some blank PDMS or other soft rubber.

2.2. **OPEN** an Eppendorf tube and place the lid on the piece of PDMS, with the inside of the lid facing up and the outside of the lid flush against the PDMS.

2.3. Carefully **PUNCH** two holes near the middle of the Eppendorf lid, through the lid and into the PDMS.

NOTE: The Eppendorf plastic is difficult to punch. This is very much an area for improvement, as the ergonomics are not ideal and the Eppendorf tube can break.

NOTE: The biopsy punch used for this process should not be used for other processes, as it is likely to be damaged during the punching. It is okay to re-use the same punch multiple times, though.

2.4. **CUT** two pieces of 6-inch Tygon® tubing.

2.5. **THREAD** one piece on tubing through one punch hole in the Eppendorf tube, and the other piece of tubing through the second punch hole. **ENSURE** one piece of tubing goes down to the bottom of the Eppendorf tube (it will eventually be submerged in solution),

while the other piece of tubing remains near the top of the tube (it will remain above the solution).

2.6. **CLOSE** the Eppendorf tube and **SEAL** around the punch holes using Teflon™ tape to make the area airtight. This is now a functioning 'reagent source vial'.

2.7. **REPEAT** steps 2.2 – 2.6 until the desired number of reagent source vials have been created.

2.8. For each reagent source vial created, **CONNECT** the end of the tubing that remained near the top of the Eppendorf tube to the splitter using a ¼-28 fitting and ferrule.

2.9. For each reagent source vial created, **CONNECT** the end of the tubing that went to the bottom of the Eppendorf tube to the desired port on the MUX distribution valve using a ¼-28 fitting and ferrule.

2.10. **CONNECT** a length of 1/16" outer diameter PEEK capillary resistance tubing to the outlet of the distribution valve using a ¼-28 fitting and ferrule.

2.11. CONNECT blank ¼-28 fittings to any unused ports on the splitter and/or distribution valve.

2.12. **PERFORM** a leak test of the reagent source vial/distribution valve system using the following steps.

2.12.1. **RETRIEVE** an empty 1.5 mL Eppendorf tube and **FILL** it with 1 mL of water.

2.12.2. **OPEN** the compressed air supply tank valve and **ROTATE** the downstream regulator to an outlet value of *50 psig*.

2.12.3. **TURN ON** the OB1 main power (the power button is on the OB1 box) and the distribution valve power (switch is on the valve box). Also **CONNECT** the distribution valve data USB cable to the computer.

2.12.4. **LAUNCH** the Elveflow software on the computer.

2.12.5. **VERIFY** the desired channel's air hose is connected from the OB1 box to the inlet port of the splitter, or **CONNECT** this, if needed.

NOTE: It doesn't matter which channel is being used for the leak test.

2.12.6. **PRESS** the *Play* button on the Elveflow software to start the OB1 system.

2.12.7. **PRESS** the *Play* button on the Elveflow software to start the distribution valve system.

2.12.8. **SET** the desired channel to *pressure control*.

2.12.9. **SET** the desired flow value to *50* (units are in mbar) and **START** the pressure.

2.12.10. **SET** the distribution valve to the desired port.

NOTE: Occasionally the distribution valve will need calibrated by **PRESSING** the *Home valve* button on the software screen. It is recommended to press this button at the beginning of each experiment, but it can also be pressed during troubleshooting if the valve doesn't fully rotate to the desired port.

2.12.11. **SUBMERGE** the Eppendorf tube with 1 mL of water in the PEEK resistance tubing coming from the outlet of the distribution valve.

2.12.12. **OBSERVE** the Eppendorf tube for the desired response: if the distribution valve is set to a port connected to a reagent source vial, bubbles should appear in

the water, indicating an airtight seal through that flow line. If the distribution valve is set to a blanked port, there should be no bubbles in the water.

NOTE: If the desired response is not observed (i.e., air bubbles are not present in in the water when the distribution valve is set to a port connected to a reagent source vial, or air bubbles are present when the distribution valve is set to a blanked port), this indicates a leak in the flow path. Begin troubleshooting by tightening the connections, re-taping the punch holes and tubing, or creating a new reagent source vial altogether. Repeat testing until the desired response is achieved.

2.12.13. **REPEAT** steps 2.12.10 – 2.12.12 for each port on the distribution valve, **ENSURING** the desired response is met for each port.

2.13. **CONNECT** the PEEK resistance tubing from the outlet of the distribution valve to the inlet of the desired flowmeter.

NOTE: The distribution valve system is now considered integral and can be left overnight or until the desired time of use. However, it is recommended to re-leak test the distribution valve system prior to actual use in order to ensure system integrity.

3. Preparation of integrated OB1 system for experiments

Once flowmeters have been calibrated, reagent source vials have been created, and the MUX distribution valve has been leak tested, the OB1 flow control system can be integrated with the flowmeters, distribution valve, and microfluidic device to autonomously control fluid flows in the microfluidic. The current version of Elveflow's OB1 flow controller software (ESI) has a beta version of an automation system, where users can create a process recipe for the connected devices to execute. This would prevent human errors as well as provide more robust and convenient control

of the system. While all the coding parameters are not detailed here, they can be found on the manufacturer website. Due to the variability of desired procedures and setups, a specific protocol is not outlined here, but this section does include general notes and best practices based on our experience with the system.

General system notes

- Once reagents have been created for a particular experiment, the reagents will be transferred to their respective reagent source vials on the distribution valve for introduction to the microfluidic device. It is recommended to prime each flow path with its respective reagent prior to connecting a piece of Tygon® tubing from the outlet of the flowmeter to the inlet of the microfluidic device and beginning the experiment. This will prevent air bubbles in the line as the valve switches between ports.
- Depending on the experiment, it may be desired that some reagents be introduced to the device and allowed to incubate for a period of time. It is recommended that during this incubation period, the valve is set to a blanked port to prevent unintentional excess flow.
    - However, the distribution valve can entrain air if the valve is switched to a blanked port without maintaining back pressure, so even if the valve is rotated to a blanked port, keep the system under pressure control and at a setpoint, such as 50 mbar.
- Both 0.6 mL and 1.5 mL Eppendorf tubes can sustain pressures of 200 mbar without popping open (a 1.5 mm biopsy hole punch was made in the top and connected to tubing on the OB1). This was expected, but just confirming.
- The largest issue we have experienced in this system is when any air gets into the distribution valve lines. Due to the surface tension differences, it is very difficult to

maintain a steady flow in the line if air is present. This is especially concerning when using small volumes of reagents in the reagent source vials and the tubing depletes the reservoir and begins to pull in air. This is an area for improvement.

ESI coding notes

- An OB1 recipe takes a user pre-defined set of operations and parameters and sets the OB1 system to those values over time.
- The available operations to be executed in a configuration are detailed on the Elveflow website, but some general information is listed below.
    - The OB1 operation sets each OB1 channel to a particular flow rate or pressure setpoint and starts/stops the flow. These setpoints, called "configurations", can be made, saved, and modified for future use.
    - The DIST operation functions to change the valve position. It has a very rapid (order of milliseconds) response.
        - Note that there is another operation in the software called MUX. This is initially confusing, but the MUX operation is not intended for use with our MUX distribution valve; Elveflow has another product that also has a MUX naming that functions with the MUX operation in the software. Use the DIST operation for rotating our distribution valve.
    - The DELAY operation has temporal accuracy up to the millisecond level, if a time delay transition is required, such as for incubation periods.
    - The GRAPH operation can be used to historize specified data for later analysis. This is especially useful for correlating with microscopy data to know when a

particular reagent was introduced to the system, as well as to confirm flow rates, etc. The graph data is saved as a file in the local computer.

- The GO operation can be used to make the recipe go to a particular step.
- The MOD operation is used to incorporate flow totalization, external de-bubblers, etc. For example, we currently use a flow integration module to incorporate the flowmeter.
- The IF operation is used to determine recipe transitions based on conditional data.
    - The MOD, IF, and GO operations are often used in tandem to create loops. The IF command is almost written backwards, saying: 'if the value does not meet the criteria, exit the If loop and continue with the recipe, or, if the value does meet the criteria, remain in the If loop and go to the next step in the loop'. A more traditional If loop would repeat the current step until the value meets the criteria and then exit the loop and continue with the recipe. This logic can be modified by including a GO operation right after the IF operation, such that the IF operation steps into the GO operation, but the GO operation forces the recipe back into the IF operation, until the IF condition has been met, in which case the code exits the loop and proceeds.
- The END operation is used to let the software know that the recipe has reached its conclusion.

- It is best practice to ensure that the final 3 steps in any recipe are: 1) an OB1 operation to set all channels to 0 pressure (or 0 flowrate) but still powered on, 2) another OB1 operation to turn all channels off, 3) an END operation. This will help prevent taring errors and let the software know when the recipe is complete.

Appendix C

MATLAB code for approximating microtubule flexural rigidity

This appendix contains the MATLAB code for iterating the flexural rigidity according to the equations detailed in the main text of this thesis, in order to compare simulated bending profiles to an actual microtubule bending profile and estimate that microtubule's flexural rigidity. Note that this code was based on MATLAB version R2019.

```
function Flexural_rigidity()

f1=figure;

C = [0  0; 1.5  -0.8; 2.5   -2.72; 3.5  -4.96; 4.5  -6.72]
%sample matrix of
%x-coordinates manually calculated along the resting lattice, with the
%respective y-coordinates designating distance deflected during bending

set(0, 'CurrentFigure', f1)
plot(C(:,1),C(:,2),'k.', 'MarkerSize',20, 'DisplayName', 'Actual MT')
hold on

microtubule_length_micrometers = 5.5; %length of microtubule in micrometers
angle_wrt_flow = 90 %angle in degrees
local_velocity = 92 %local velocity in um/s

microtubule_length = microtubule_length_micrometers() * 1E-6;  %length of microtubule in
meters
counter = 1; %starting a counter for the For loop
kcounter = 1; %starting a second counter for the For loop
control_y = zeros(1,10*length(microtubule_length)); %pre-allocating variable for speed

for k = 1E-24:1E-24:9E-24 %iterating the value of flexural rigidity, k
  for x = 0:0.1E-6:microtubule_length %for each value of k, create a sample 'microtubule' the
same length as the real microtubule
  control_y(counter) =
(((pi*(0.0006922)*abs(sind(angle_wrt_flow))*(local_velocity)*((microtubule_length)^4))/(6*k*
log(microtubule_length/(2*25E-9)))))*(((x/microtubule_length)^4)-
```

```
4*((x/microtubule_length)^3)+6*((x/microtubule_length)^2)); %our equation for using the x-coordinates and the value of k to yield y-coordinates and a subsequent bending curve
  counter = counter+1;
  end

  control_y=control_y.*-1;
  forlegend1 = num2str(k);
  forlegend2 = 'N*m^{2}';
  scatter(0:0.1:microtubule_length_micrometers(),control_y()) %plot the sample bending curves
  hold on
  clear control_y;
  legendcounter(kcounter) = k;
  kcounter = kcounter+1;
  counter = 1;
end

legend('FontSize', 16);
legend('Actual MT Curvature','1E-24 N*m^{2}','2E-24 N*m^{2}','3E-24 N*m^{2}','4E-24 N*m^{2}','5E-24 N*m^{2}','6E-24 N*m^{2}','7E-24 N*m^{2}','8E-24 N*m^{2}','9E-24 N*m^{2}'); %manually coding the legend; will need to be changed if the k-value range is changed
legend('Location','southwest');
title(legend,'Values of Flexural Rigidity');
xlabel('Point along the microtubule length (\mum)', 'FontSize', 14);
ylabel('Distance that the associated point deflected (\mum)', 'FontSize', 14);
end
```